

# Brain atrophy in prodromal synucleinopathy is shaped by structural connectivity and gene expression

Shady Rahayel,<sup>1,2</sup> Christina Tremblay,<sup>1</sup> Andrew Vo,<sup>1</sup> Ying-Qiu Zheng,<sup>3</sup> Stéphane Lehericy,<sup>4</sup> Isabelle Arnulf,<sup>4</sup> Marie Vidailhet,<sup>4</sup> Jean-Christophe Corvol,<sup>4</sup> ICEBERG Study Group,<sup>4</sup> Jean-François Gagnon,<sup>2,5,6</sup> Ronald B. Postuma,<sup>2,7</sup> Jacques Montplaisir,<sup>2,8</sup> Simon Lewis,<sup>9</sup> Elie Matar,<sup>9</sup> Kaylena Ehgoetz Martens,<sup>9,10</sup> Per Borghammer,<sup>11</sup> Karoline Knudsen,<sup>11</sup> Allan Hansen,<sup>11</sup> Oury Monchi,<sup>6,12</sup> Bratislav Misic<sup>1,†</sup> and Alain Dagher<sup>1,†</sup>

<sup>†</sup>These authors contributed equally to this work.

## Abstract

Isolated REM sleep behaviour disorder (iRBD) is a synucleinopathy characterized by abnormal behaviours and vocalizations during REM sleep. Most iRBD patients develop dementia with Lewy bodies, Parkinson's disease, or multiple system atrophy over time. Patients with iRBD exhibit brain atrophy patterns that are reminiscent of those observed in overt synucleinopathies. However, the mechanisms linking brain atrophy to the underlying alpha-synuclein pathophysiology are poorly understood. Our objective was to investigate how the prion-like and regional vulnerability hypotheses of alpha-synuclein might explain brain atrophy in iRBD.

Using a multicentric cohort of 182 polysomnography-confirmed iRBD patients who underwent T1-weighted MRI, we performed vertex-based cortical surface and deformation-based morphometry analyses to quantify brain atrophy in patients (67.8 years, 84% men) and 261 healthy controls (66.2 years, 75%) and investigated the morphological correlates of motor and cognitive functioning in iRBD. Next, we applied the agent-based Susceptible-Infected-Removed model (i.e., a computational model that simulates in silico the spread of pathologic alpha-synuclein based on structural connectivity and gene expression) and tested if it recreated atrophy in iRBD by statistically comparing simulated regional brain atrophy to the atrophy observed in patients. The impact of *SNCA* and *GBA*

gene expression and brain connectivity was then evaluated by comparing the model fit to the one obtained in null models where either gene expression or connectivity was randomized.

The results showed that iRBD patients present with cortical thinning and tissue deformation, which correlated with motor and cognitive functioning. Next, we found that the atrophy simulated based on brain connectivity and gene expression recreated cortical thinning ( $r=0.51$ ,  $p=0.0007$ ) and tissue deformation ( $r=0.52$ ,  $p=0.0005$ ) in patients, and that the connectome's architecture along with *SNCA* and *GBA* gene expression contributed to shaping atrophy in iRBD. We further demonstrated that the full agent-based model performed better than network measures or gene expression alone in recreating the atrophy pattern in iRBD.

In summary, atrophy in iRBD is extensive, correlates with motor and cognitive functioning, and can be recreated using the dynamics of agent-based modelling, structural connectivity, and gene expression. These findings support the concepts that both prion-like spread and regional susceptibility account for the atrophy observed in prodromal synucleinopathies. Therefore, the agent-based Susceptible-Infected-Removed model may be a useful tool for testing hypotheses underlying neurodegenerative diseases and new therapies aimed at slowing or stopping the spread of alpha-synuclein pathology.

#### **Author affiliations:**

1 The Neuro (Montreal Neurological Institute-Hospital), McGill University, Montreal H3A 2B4, Canada

2 Centre for Advanced Research in Sleep Medicine, Hôpital du Sacré-Cœur de Montréal, Montreal H4J 1C5, Montreal, Canada

3 Wellcome Centre for Integrative Neuroimaging, Centre for Functional Magnetic Resonance Imaging of the Brain, University of Oxford, John Radcliffe Hospital, Oxford OX3 9DU, United Kingdom

3 Sorbonne Université, Institut du Cerveau – Paris Brain Institute – ICM, INSERM, CNRS, Assistance Publique Hôpitaux de Paris, Pitié-Salpêtrière Hospital, Paris 75013, France

4 Department of Psychology, Université du Québec à Montréal, Montreal H2X 3P2, Canada

5 Research Centre, Institut universitaire de gériatrie de Montréal, Montreal H3W 1W5, Canada

6 Department of Neurology, Montreal General Hospital, Montreal H3G 1A4, Canada

7 Department of Psychiatry, Université de Montréal, Montreal H3T 1J4, Canada

8 ForeFront Parkinson's Disease Research Clinic, Brain and Mind Centre, University of Sydney, Camperdown NSW 2050, Australia

9 Department of Kinesiology and Health Sciences, University of Waterloo, Waterloo N2L 3G1, Canada

10 Department of Nuclear Medicine and PET, Aarhus University Hospital, Aarhus DK-8200, Denmark

11 Departments of Clinical Neurosciences, Radiology, and Hotchkiss Brain Institute, University of Calgary, Calgary T2N 4N1, Canada

Correspondence to: Shady Rahayel, PhD

The Neuro (Montreal Neurological Institute-Hospital), McGill University

3801 University Street, Montreal, Quebec, Canada, H3A 2B4

[shady.rahayel@mcgill.ca](mailto:shady.rahayel@mcgill.ca)

**Running title:** Agent-based modelling of atrophy in iRBD

**Keywords:** REM sleep behaviour disorder, Parkinson's disease, dementia with Lewy bodies, alpha-synuclein, MRI

**Abbreviations:** iRBD = isolated REM sleep behaviour disorder; MDS-UPDRS-III = Movement Disorders Society–Unified Parkinson's disease Rating Scale, motor

examination; MoCA = Montreal Cognitive Assessment; SIR = Susceptible-Infected-Removed

## Introduction

Isolated REM sleep behaviour disorder (iRBD) is characterized by abnormal motor behaviours and vocalizations during REM sleep.<sup>1,2</sup> iRBD typically develops into dementia with Lewy bodies, Parkinson's disease or multiple system atrophy,<sup>3</sup> making it an early manifestation and phenotype of synucleinopathies. Specifically, iRBD is thought to result from the impairment of brainstem circuits involved in REM sleep muscle atonia that occurs as a result of early accumulation of pathologic alpha-synuclein in the pontine tegmentum.<sup>4,5</sup> However, MRI studies in patients with polysomnography-proven iRBD without cognitive or motor diagnoses have also shown patterns of diffuse brain atrophy reminiscent of dementia with Lewy bodies or Parkinson's disease.<sup>6,7</sup> Moreover, the severity of cortical atrophy is a predictor of subsequent dementia, hence more severe disease.<sup>8</sup>

Dementia with Lewy bodies and Parkinson's disease are thought to arise from the accumulation of misfolded alpha-synuclein in the brain.<sup>9</sup> Previous pathological brain staging schemes have suggested that the toxic agent starts in the brainstem and then spreads upwards,<sup>10,11</sup> giving rise to the clinical features that lead to a dementia- or a parkinsonism-first phenoconversion in iRBD patients. Evidence from animal models shows that pathologic alpha-synuclein can propagate and promote protein misfolding, supporting the prion-like model of alpha-synuclein.<sup>4,12-17</sup> In line with this, MRI studies performed in patients with Parkinson's disease also show that atrophy patterns are shaped by connectivity.<sup>18-20</sup>

We previously modelled alpha-synuclein propagation using a Susceptible-Infected-Removed (SIR) model,<sup>21</sup> a computational model based on an adaptation of epidemiological SIR models but applied to neurological diseases with the underlying hypothesis that alpha-

synuclein propagation works like an infection in a population. In this model, every agent is an autonomous alpha-synuclein molecule that can exist in three states: Susceptible (normal), Infected (misfolded) or Removed (degraded). In its misfolded state, the agent becomes infective. Agents can also move between regions via neural connections. The model uses *SNCA* and *GBA* gene expression as measures of local alpha-synuclein concentration, and connectivity to determine agent numbers and propagation. The model has predicted atrophy distribution in Parkinson's disease patients and alpha-synuclein distribution in a mouse model.<sup>21,22</sup> Null models show that both connectivity and local alpha-synuclein concentration are important factors shaping the propagation of agents.<sup>21,22</sup> However, it remains unknown if these mechanisms also explain the atrophy seen in early synucleinopathies.

In this study, we compiled neuroimaging data from several centres to generate a map of brain atrophy in iRBD. We then used the agent-based SIR model to test if brain connectivity and *SNCA* and *GBA* gene expression explain brain atrophy patterns in iRBD. Vertex-based cortical surface and deformation-based morphometry analyses were performed in 182 polysomnography-confirmed iRBD patients and 261 healthy controls who underwent T1-weighted brain MRI to characterize atrophy and investigate the correlates of motor and cognitive functioning. We then tested whether brain connectivity and gene expression recreated atrophy by simulating atrophy with the SIR model and by statistically comparing the simulated pattern to the actual atrophy pattern found in iRBD. We next used null modelling to test if connectivity and gene expression were decisive in shaping the brain atrophy seen in iRBD. We hypothesized that the SIR model would recreate brain atrophy in iRBD and that both connectivity and gene expression would be significant determinants of atrophy.

# Materials and methods

## Participants

A total of 443 participants (182 iRBD patients and 261 controls) were recruited from five sites: 116 (59 patients) from the Movement Disorders clinic at the Hôpital de la Pitié-Salpêtrière (France), 83 (48 patients) from the Centre for Advanced Research on Sleep Medicine at the Hôpital du Sacré-Cœur de Montréal (Canada), 56 (30 patients) from the ForeFront Parkinson's Disease Research Clinic at the University of Sydney (Australia), 38 (18 patients) from Aarhus University Hospital (Denmark), and 150 (27 patients) from the Parkinson's Progression Markers Initiative baseline cohort.<sup>23</sup> All iRBD patients had a polysomnography-confirmed diagnosis of iRBD and were free of parkinsonism and dementia at the clinical examination closest in time to MRI.<sup>24,25</sup> An overview of the study protocol along with a flowchart of the selected patients are presented in Figure 1 and the cohorts' demographics are available in Supplementary Table 1. All participants were part of research protocols approved by local ethics committees and provided written informed consent. The current project was also approved by the Research Ethics Board of the McGill University Health Centre.

## MRI

### MRI acquisition

The Montreal cohort underwent T1-weighted imaging with a 3T Siemens TIM Trio scanner with a 12-channel head coil, MPRAGE sequence: TR: 2,300 ms, TE: 2.91 ms, flip angle: 9°, and voxel size: 1 mm<sup>3</sup> isotropic. The Paris cohort underwent T1-weighted imaging with a 3T Siemens TIM Trio scanner with a 12-channel head coil, MPRAGE sequence: TR: 2,300 ms, TE: 4.18 ms, TI: 900 ms, flip angle: 9°, and voxel size: 1 mm<sup>3</sup> isotropic; or a 3T PRISMA Fit scanner with a 64-channel head coil, MP2RAGE sequence: TR: 5,000 ms, TE: 2.98 ms, TI: 700 and 2,500 ms, flip angle: 4° and 5°, GRAPPA: 3, and voxel size: 1 mm<sup>3</sup> isotropic. The Sydney cohort was imaged with a GE Discovery MR750 3T scanner

with an 8-channel head coil, BRAVO sequence: TR: 5,800 ms, TE: 2.6 ms, flip angle: 12°, and voxel size: 1 mm<sup>3</sup> isotropic. The Aarhus cohort was imaged with a 3T Siemens MAGNETOM Skyra scanner with a 32-channel head coil, MPRAGE sequence: TR: 2,420 ms, TE: 3.7 ms, TI: 960 ms, flip angle: 9°, and voxel size: 1 mm<sup>3</sup> isotropic. The T1-weighted images from the Parkinson's Progression Markers Initiative cohort, an international multicentre cohort, were also included (see [www.ppmi-info.org](http://www.ppmi-info.org) for the imaging protocols).<sup>23</sup>

## Quantification of atrophy

Deformation-based morphometry was performed using CAT12 (version 12.7; [www.neuro.uni-jena.de/cat](http://www.neuro.uni-jena.de/cat)) to quantify atrophy by measuring the non-linear change required in every voxel for registering the brain to the common template.<sup>26</sup> The processing included bias correction, affine registration, unified segmentation,<sup>27</sup> skull-stripping, parcellation, intensity transformation, partial volume estimation, and spatial normalization using DARTEL.<sup>26</sup> This resulted in whole-brain maps of Jacobian determinants, which were smoothed with a 12-mm isotropic kernel and then used as the measure of local brain atrophy. Images with an automated quality rating below 80% were excluded from analyses involving deformation-based morphometry.

Brain atrophy in iRBD also manifests as abnormal cortical thickness and surface area.<sup>28</sup> To ensure that findings were not due to the atrophy metric, the scans passing deformation-based morphometry quality control were also processed with FreeSurfer (version 6.0.0) to generate individual thickness and surface area maps of the whole cortex.<sup>29,30</sup> Every map was inspected by a trained rater (S.R.) and a score from 1-4 was assigned to each scan based on published guidelines,<sup>31,32</sup> scans with a score >2 (i.e., major reconstruction errors) were excluded from cortical surface analyses.

## W-scoring and brain parcellation

For deformation-based morphometry-derived atrophy, a *W*-score map was computed from each patient's smoothed map by regressing out the effects of age, sex, and site found in the age- and sex-matched controls passing quality control.<sup>33</sup> At each voxel, the following formula was applied:

$$W\text{-score} = \frac{(\text{iRBD raw value} - \text{control value expected for the patient's age, sex, and site})}{\text{SD of the residuals in controls}} \quad (1)$$

A voxel with a negative *W*-score represents greater atrophy (decreased volume) in the iRBD patient compared to controls, whereas a positive *W*-score indicates less atrophy (increased volume), while considering the confounds.

Regional *W*-scores were then extracted by parcellating every map with a 42-region atlas for which corresponding structural connectivity and gene expression data were available.<sup>21</sup> This atlas comprised 34 cortical regions from the Desikan-Killiany atlas and 7 subcortical regions from FreeSurfer.<sup>34,35</sup> Due to its importance in synucleinopathies,<sup>36,37</sup> the substantia nigra was added from the 7-tesla “Atlas of the basal ganglia” (ATAG atlas).<sup>38</sup> The 42 regional *W*-scores extracted from each map were then averaged across iRBD patients to yield 42 *W*-scores representing regional tissue deformation. *W*-scores were also extracted using finer parcellations of 65 and 119 regions to ensure that findings were robust to parcellation resolution. Because gene expression data, used by the model for determining regional alpha-synuclein synthesis and clearance (see below), were only available in the right hemisphere for 2 of the 6 existing post-mortem brains,<sup>39</sup> and because diffusion tractography-based reconstruction of the connectome often leads to inaccurate measurements of interhemispheric connections,<sup>40,41</sup> the main analyses were performed in the left hemisphere.

For cortical surface analysis, thickness and surface area values were extracted from each surface from the same 34 cortical regions as used for deformation-based morphometry.<sup>34</sup> Since subcortical regions do not have a cortical surface from which to derive thickness and area values, the global volume measurement generated as part of FreeSurfer's subcortical processing was used. The substantia nigra was excluded from cortical surface analyses as it is unavailable in FreeSurfer, resulting in a total of 41 regions. Since cortical surface area and subcortical volume scale with head size,<sup>42,43</sup> the raw values were divided by the estimated total intracranial volume (derived from FreeSurfer). The same *W*-scoring procedure was then applied to these values to adjust for the effects of age, sex, and site from controls who passed quality control. To ascertain those findings were not due to the multicentric nature of the cohort, we also tested the model with harmonized regional *W*-scores derived from the ComBat harmonization method,<sup>44-46</sup> a batch-effect correction tool used in genomics and validated for neuroimaging that removes the unwanted scanning-related inter-site variability while preserving biological variability.

Importantly, to facilitate interpretation when testing the model, the *W*-scores were inverted such that a positive score indicated a region with greater atrophy and a negative score indicated lower atrophy in iRBD patients compared to controls.

## Agent-based SIR model

### Model overview

The agent-based SIR model ([https://github.com/yingqiuz/SIR\\_simulator](https://github.com/yingqiuz/SIR_simulator)) was used to simulate the spread of alpha-synuclein.<sup>21</sup> This algorithm applies agent-based modelling inside an SIR framework to model the spread as an epidemic shaped by the simultaneous effect of brain connectivity along with *SNCA* and *GBA* expression.<sup>21</sup> This model previously recreated the atrophy observed in Parkinson's disease and frontotemporal dementia.<sup>21,47</sup> In this model, every agent is an autonomous alpha-synuclein molecule that belongs to one of three mutually exclusive states: the "Susceptible" state when the agent is normal (normal

alpha-synuclein), the “Infected” state when the agent becomes infective (misfolded alpha-synuclein isoform), and the “Removed” state when the agent is degraded. Agents can also move between regions via neural connections. The transitions between states are determined by rules guiding the interaction dynamics between agents and their regional environment. The model simulates atrophy in every brain region based on the following computational steps: 1) the production of normal alpha-synuclein, 2) the clearance of normal and misfolded alpha-synuclein, 3) the misfolding of normal alpha-synuclein, 4) the propagation of normal and misfolded alpha-synuclein, and 5) the emergence of atrophy.

## Connectivity and gene data

The details of diffusion-weighted image processing, deterministic fibre tracking, and gene expression data have been described elsewhere.<sup>21</sup> Briefly, the structural connectivity data were used to model the spread of agents from one region to another; they were derived from the pre-processed diffusion-weighted images of 1,027 participants from the Human Connectome Project.<sup>61</sup> Deterministic tractography was used to construct consensus connectivity matrices between the 42 regions as described previously.<sup>48-50</sup> The analysis was performed at connection densities of 25%, 30%, 35%, and 40% to ensure that results were robust to change in this parameter. A distance matrix of the mean Euclidean length of the corresponding streamlines for the 42 regions was also generated to modulate the rate of movement of agents between connected regions. For the gene expression data, the regional expression of *SNCA* and *GBA* were used to model the regional synthesis and clearance of alpha-synuclein; values were derived from the post-mortem mRNA transcription profiles of 6 subjects from the Allen Human Brain Atlas<sup>39</sup> using *abagen* (<https://abagen.readthedocs.io/en/stable/>)<sup>51</sup> and averaged for the 42 regions.

## Production of normal alpha-synuclein (module 1)

In region  $i$ , the synthesis of susceptible agents per unit time occurs with probability  $\alpha_i$ :

$$\alpha_i = \Phi_{0,1}(SNCAexpression_i) \quad (2)$$

where  $\Phi_{0,1}(\cdot)$  is the standard normal cumulative distribution function and  $SNCAexpression_i$  is the gene expression of *SNCA* of region  $i$ . At each timestep, the increment of susceptible agents in region  $i$  is  $\alpha_i S_i \Delta t$ , where  $S_i$  is the size of region  $i$  and  $\Delta t$  is the total time.

### Clearance of normal and misfolded alpha-synuclein (module 2)

In region  $i$ , the clearance of susceptible and infected agents per unit time occurs with probability  $\beta_i$ :

$$\beta_i = \Phi_{0,1}(GBAexpression_i) \quad (3)$$

where  $GBAexpression_i$  is the gene expression of *GBA* of region  $i$ . Considering that the probability that an agent is still active after  $\Delta t$  is given by  $\lim_{\delta\tau \rightarrow 0} (1 - \beta\delta\tau)^{\Delta t/\delta\tau} = e^{-\beta\Delta t}$ , the cleared proportion within  $\Delta t$  is  $1 - e^{-\beta\Delta t}$ .

### Misfolding of normal alpha-synuclein (module 3)

The susceptible agents not cleared from region  $i$  may become infected per unit time with probability  $\gamma_i$ :

$$\gamma_i = 1 - e^{M_i \ln(1-\gamma_i^0)} \quad (4)$$

where  $M_i$  is the population of infected agents in region  $i$  and  $\gamma_i^0$  is the baseline likelihood that a susceptible agent becomes an infected agent in region  $i$ , which was set as the reciprocal of region size. The probability that a susceptible agent did not get infected is given by  $(1 - \gamma_i^0)^{M_i}$ ; therefore,  $\gamma_i = 1 - (1 - \gamma_i^0)^{M_i} = 1 - e^{M_i \ln(1-\gamma_i^0)}$  represents the probability that a susceptible agent becomes infected in region  $i$  per unit time. Similarly, the probability that an agent is still susceptible after  $\Delta t$  is given by  $\lim_{\delta\tau \rightarrow 0} (1 -$

$\gamma_i^0 \delta \tau)^{M_i \Delta t / \delta \tau} = e^{-\gamma_i^0 M_i \Delta t}$ , with the proportion of agents becoming infected after  $\Delta t$  being  $1 - e^{-\gamma_i^0 M_i \Delta t}$ .

To determine the baseline density of susceptible agents in every region, the population of susceptible agents  $N_i$  is incremented with:

$$\Delta N_i = \alpha_i S_i \Delta t - (1 - e^{-\beta_i \Delta t}) N_i \quad (5)$$

Once the system reaches its stable point (error tolerance  $\varepsilon < 10^{-7}$ ), the pathogenic spread and update of  $N_i$  and  $M_i$  is given by:

$$\Delta N_i = \alpha_i S_i \Delta t - (1 - e^{-\beta_i \Delta t}) N_i - (e^{-\beta_i \Delta t})(1 - e^{-\gamma_i^0 M_i \Delta t}) N_i \quad (6)$$

$$\Delta M_i = (e^{-\beta_i \Delta t})(1 - e^{-\gamma_i^0 M_i \Delta t}) N_i - (1 - e^{-\beta_i \Delta t}) M_i \quad (7)$$

#### Propagation of normal and misfolded alpha-synuclein (module 4)

Susceptible and infected agents in region  $i$  either remain in region  $i$  or spread to other regions based on a multinomial distribution per unit time with probabilities:

$$P_{region_i \rightarrow region_i} = \rho_i \quad (8)$$

$$P_{region_i \rightarrow edge_{ij}} = (1 - \rho_i) \frac{w_{ij}}{\sum_j w_{ij}} \quad (9)$$

where  $w_{ij}$  is the connection strength between regions  $i$  and  $j$  and  $\rho_i$  is the probability that an agent remains in region  $i$ . The main analyses were performed using  $\rho=0.5$  for all regions, but  $\rho$  values from 0.1 to 0.9 were also tested to ensure that findings did not depend solely on this parameter.

The susceptible and infected agents located inside an edge could exit the edge per unit time based on binary probabilities:

$$P_{edge_{ij} \rightarrow region_j} = \frac{1}{l_{ij}} \quad (10)$$

$$P_{edge_{ij} \rightarrow edge_{ij}} = 1 - \frac{1}{l_{ij}} \quad (11)$$

where  $l_{ij}$  is the length of the edge between regions  $i$  and  $j$ . The increment in  $N_i$  and  $M_i$  in region  $i$  after total time  $\Delta t$  is given by:

$$\Delta N_i = \sum_j \frac{1}{l_{ji}} N_{ji} \Delta t - (1 - \rho_i) N_i \Delta t \quad (12)$$

$$\Delta M_i = \sum_j \frac{1}{l_{ji}} M_{ji} \Delta t - (1 - \rho_i) M_i \Delta t \quad (13)$$

whereas the increment in the population of susceptible and infected agents inside the edge between regions  $i$  and  $j$  ( $N_{ij}$  and  $M_{ij}$ , respectively) after total time  $\Delta t$  is:

$$\Delta N_{ij} = (1 - \rho_i) \frac{w_{ij}}{\sum_j w_{ij}} N_i \Delta t - \frac{1}{l_{ij}} N_{ij} \Delta t \quad (14)$$

$$\Delta M_{ij} = (1 - \rho_i) \frac{w_{ij}}{\sum_j w_{ij}} M_i \Delta t - \frac{1}{l_{ij}} M_{ij} \Delta t \quad (15)$$

### Emergence of simulated atrophy (module 5)

Regional atrophy was simulated as the sum of two processes: the direct toxicity resulting from the regional accumulation of infected agents and the deafferentation caused by cell death in connected regions. In region  $i$ , the atrophy accrual is given by:

$$\Delta L_i(t) = k_1 (1 - e^{-r_i(t)\Delta t}) + k_2 \sum_j \frac{w_{ji}}{\sum_j w_{ji}} (1 - e^{-r_j(t-1)\Delta t}) \quad (16)$$

where  $r_i(t)$  is the proportion of infected agents in region  $i$  at time  $t$  and  $1 - e^{-r_i(t)\Delta t}$  is the increment of atrophy at time  $t$  caused by the accumulation of alpha-synuclein pathology within  $\Delta t$ . The first term controls the direct impact of infected agents, whereas the second term weighs the increment of atrophy based on deafferentation from neighbouring regions. Each term was given a weight  $k_1$  and  $k_2$  of 0.5 for the main analyses, but weights varying from 0.1 to 0.9 were also tested to ensure that findings were not due to this parameter only. In other words, this module generated, at every timestep, a value of simulated atrophy for each of the 42 regions; it is this simulated atrophy that was correlated with the observed atrophy to test if the model accurately recreated the brain atrophy of iRBD.

## Statistical analysis

### Between group differences in atrophy

For deformation-based morphometry-derived tissue deformation, two-tailed general linear models with age, sex, and site as covariates were performed to investigate the presence of significant differences between iRBD patients and controls. The Benjamini-Hochberg

procedure was used to correct for the rate of false discoveries at a statistical threshold of  $p < 0.05$ .<sup>52</sup>

For surface-based cortical measurements, general linear models were performed at each vertex to investigate the presence of significant differences in cortical thickness or surface area in iRBD patients compared to controls. Surface maps were smoothed using a 15-mm full-width, half-maximum kernel and age, sex, and site were entered as covariates, as well as estimated total intracranial volume for surface area. The surface correlates of motor and cognitive functioning in iRBD were also investigated in participants with available Movement Disorders Society–Unified Parkinson’s Disease Rating Scale, part III (MDS-UPDRS-III; 90 patients, 130 controls) or Montreal Cognitive Assessment (MoCA; 134 patients, 174 controls) scores. Using age, sex, and site (and total intracranial volume for cortical surface area) as covariates, vertex-based analyses were performed to investigate the vertices significantly correlated with clinical variables. Another contrast matrix was also created to identify the vertices where thickness and area correlations with the MDS-UPDRS-III or MoCA scores differed significantly between iRBD patients and controls. Statistical significance was determined by Monte Carlo simulation at a corrected threshold of  $p < 0.05$ .

### **Replication of observed atrophy**

To assess if the model recreated atrophy, the spread of pathologic alpha-synuclein was simulated in silico by injecting pathology in one region, simulating the propagation over 10,000 timesteps, and repeating the process for every region as seed. At each timestep, the model generated regional values representing the amount of simulated atrophy and the simulated number of infected and susceptible agents. To avoid interpreting any spurious overfit of the model when assessing the fit between atrophy patterns, since some regions may act as outliers due to agents being present in only a few brain regions when initiating the spread, we discarded all the timesteps where the number of infected agents in any region increased by more than 1% compared to the previous timestep.

At each timestep, Spearman's rank correlations were used to assess the association between simulated atrophy and observed atrophy in patients. The highest correlation coefficient, if statistically significant at  $p < 0.05$ , was considered as the peak fit. Since thickness  $W$ -scores correlated with region size ( $r = 0.54$ ,  $p = 0.0013$ ), the scores were divided by the region size before assessing the peak fit. For cortical surface measurements, the peak fit was also assessed over the 34 cortical regions only to ensure that the peak fit was not due to the presence of subcortical volume measurements. The *ggseg* package was used for visualization.<sup>53</sup>

### **Comparison with other model-derived, topological, and gene metrics**

To determine that connectomics or regional vulnerability alone did not explain the atrophy patterns of iRBD, we tested whether simpler measures predicted brain atrophy as well as the complete agent-based model. These measures included (1) model-derived measurements representing the number of infected and susceptible agents at each timestep in each region; (2) network measures alone, namely node degree, node strength, node betweenness centrality and eigenvector centrality, derived from the Brain Connectivity Toolbox ([www.sites.google.com/site/bctnet/](http://www.sites.google.com/site/bctnet/));<sup>54</sup> (3) *SNCA* and *GBA* regional expression alone. Node degree represented the number of edges (structural connections) connected to a node (region). Node strength represented the sum of the weights of the edges connected to the node. Node betweenness centrality represented the number of times a given node was found in the shortest paths linking every node pair in the network. Eigenvector centrality was a self-referential measure of centrality; nodes with high eigenvector centrality connected with other nodes that also had high eigenvector centrality. Node betweenness centrality and eigenvector centrality tested whether hub regions were more sensitive to disease.

## Randomized null models

To test if brain connectivity and gene expression shaped the atrophy in iRBD, all fits between atrophy patterns were tested against null models in which network topology and geometry or gene expression was randomized. For the connectome, rewired and repositioned null models were used to assess network topology and/or geometry. Rewired null models are models in which structural connectivity pairs of regions were randomized while preserving the network's original degree sequence and density. Swapping of the connectivity and distance matrices was performed using the Maslov-Sneppen algorithm in the Brain Connectivity Toolbox.<sup>54,55</sup> The randomized matrix was inserted into the model to derive a null peak fit between atrophy patterns; this process was repeated 10,000 times for generating a distribution of null peak fits, to the average of which the empirical peak fit between atrophy patterns was statistically compared. An unbiased Monte-Carlo estimate of the exact  $p$ -value was used to assess significance. The same steps were repeated using repositioned null models, i.e., models in which the spatial position of regions was randomized while preserving the network's original degree sequence and connection profile. The same approach was also conducted for gene expression, where distinct null models were generated with either *SNCA* or *GBA* regional expression randomized between the 42 regions.

## Data availability

The agent-based SIR model is available at [https://github.com/yingqiuz/SIR\\_simulator](https://github.com/yingqiuz/SIR_simulator). The regional values of the tissue deformation, cortical thickness, and cortical surface area maps are available at <https://github.com/srahayel/SIR-RBD>.

## Results

### Demographics

Of the 443 participants, 34 did not pass deformation-based morphometry quality control, resulting in 409 participants (171 patients and 238 controls). There were no significant differences in age (iRBD:  $67.7 \pm 6.6$  years; controls:  $66.6 \pm 7.9$ ,  $p=0.11$ ) and sex (iRBD:

83% men, controls: 77% men,  $p=0.13$ ) between groups, but patients had higher MDS-UPDRS-III scores ( $p<0.001$ ) and lower MoCA scores ( $p<0.001$ ) (Table 1). Of these 409 participants, 64 did not pass FreeSurfer quality control, resulting in 345 participants (138 iRBD patients and 207 controls) for quantifying cortical thickness and surface area differences. There were no significant differences in age (iRBD:  $66.2 \pm 7.6$  years; controls:  $67.0 \pm 6.3$  years;  $p=0.28$ ) and sex (iRBD: 81% men, controls: 77% men;  $p=0.34$ ) for this sample.

### **iRBD patients show brain atrophy.**

We investigated if this iRBD cohort showed brain atrophy compared to controls. In terms of deformation-based morphometry-derived tissue deformation, patients had decreased volume in the left middle temporal cortex, cuneus, lingual gyrus, fusiform gyrus, banks of the superior temporal sulcus and the pericalcarine area, and increased volume in the insula compared to controls; in the right hemisphere, decreased volume was found in the precentral, supramarginal, superior and middle temporal, lingual, and cuneus regions. However, only the left middle temporal region was significant after correction ( $p_{FDR}=0.045$ ) (Fig. 2A and Supplementary Table 2).

For cortical thickness, patients showed significant thinning compared to controls in two clusters in the left hemisphere, namely one posterior cluster that included the posterior temporal and inferior parietal cortices and another cluster that extended from the dorsolateral prefrontal cortex to the orbitofrontal cortex, and in one cluster in the right hemisphere, which included the posterior temporal and lateral occipital cortices (Fig. 3A and Table 2). Compared to controls, patients also had significantly increased cortical surface area in the left inferior temporal cortex and sulcus that extended to the entorhinal cortex (Fig. 3B and Table 2). These findings demonstrate the presence of brain atrophy in iRBD.

## **Brain atrophy in iRBD is associated with motor and cognitive functioning.**

In iRBD patients, higher MDS-UPDRS-III scores were associated with cortical thinning in the bilateral frontal cortex and the right temporal cortex, and with increased thickness in the right sensorimotor cortex (Fig. 4B and Table 2). Higher MDS-UPDRS-III scores were also associated with increased cortical surface area in the bilateral occipital cortex, the left inferior parietal cortex, and the right posterior temporal cortex (Fig. 4B and Table 2). The associations with MDS-UPDRS-III scores were significantly different between iRBD patients and controls, with the correlation being stronger in patients in the bilateral sensorimotor cortex for thickness and in the frontopolar, sensorimotor, occipital, inferior parietal, and lingual and fusiform cortices for surface area (Fig. 4B and Table 2). For the MoCA, lower scores were associated with cortical thinning in the bilateral insula, the right temporal cortex, and the left posterior temporal cortex (Fig. 4C and Table 2). MoCA scores were not associated with cortical surface area in iRBD patients and there were no differences in correlation slopes between patients and controls.

## **The SIR model recreates the atrophy of iRBD.**

The agent-based model was then applied to simulate alpha-synuclein spread and generate patterns of simulated atrophy in every region. We found that the model recreated the deformation-based morphometry-derived tissue deformation pattern, with the peak fit reaching  $r=0.52$  ( $p<0.0005$ ) when seeding from the banks of superior temporal sulcus at a connection density of 40% (Fig. 2B). The fit between atrophy patterns increased gradually with each timestep to reach a peak, followed by a decline (Fig. 2C). At the peak, the simulated atrophy was most prominent in the pericalcarine cortex, accumbens, cuneus, substantia nigra, amygdala, and the banks of the superior temporal sulcus (Fig. 2C). At later timesteps, the correlation declined but simulated atrophy was seen in putamen and lingual gyrus. The model also recreated atrophy at the lower connection densities ( $r=0.44$  at 35%,  $r=0.50$  at 30%,  $r=0.36$  at 25%) (Supplementary Fig. 1).

Similarly, the model recreated cortical atrophy, derived from FreeSurfer, with peak fits reaching  $r=0.51$  ( $p=0.0007$ ) for cortical thickness (Fig. 3C) and  $r=0.43$  ( $p=0.006$ ) for cortical surface area. However, when assessing the fit over the 34 cortical regions only (without the subcortical measurements), only thickness remained significant ( $r_{thickness}=0.48$ ,  $p=0.004$ ;  $r_{area}=0.28$ ,  $p=0.11$ ). The fit for cortical thickness increased gradually and reached its peak once the system had attained the equilibrium state; at this timestep, the simulated atrophy was primarily found in the frontal pole, amygdala, accumbens, and entorhinal cortex (Fig. 3D). The fit was also significant at lower connection densities ( $r=0.50$  at 35%,  $r=0.49$  at 30%,  $r=0.48$  at 25%).

To confirm that our findings were not caused by site-specific variability, the tissue deformation and cortical thickness  $W$ -scores were harmonized using ComBat<sup>44,45</sup>; the model recreated the patterns just described in a similar way ( $r=0.515$ ,  $p=5.69 \times 10^{-4}$  for tissue deformation,  $r=0.523$ ,  $p=5.50 \times 10^{-4}$  for cortical thickness). In addition, the model also recreated atrophy when using finer parcellations of 65 and 119 regions (Supplementary Fig. 2), with various spreading rates of agents (Supplementary Fig. 3), and with different weights given to misfolded alpha-synuclein accumulation versus deafferentation in the simulated atrophy ratio, with higher peak fits obtained when deafferentation was given the larger weight (Supplementary Fig. 4). Taken together, these results demonstrate that volume and cortical thickness atrophy in iRBD can be recreated based on agent-based modelling utilizing connectivity and gene expression for generation of the model.

## **Simulated atrophy outperforms gene and network metrics.**

To ascertain whether brain connectivity or gene expression alone could recreate the atrophy pattern as well as the full model, we also tested several network-based and other model-derived measures. For every connection density, we found that the simulated atrophy from the agent-based model measure always yielded the highest peak fits ( $r=0.52$ ,  $p<0.0005$  at 40%), followed by the number of susceptible agents ( $r=0.32$ ,  $p=0.039$ ) (Fig. 5). None of the other measures, namely the number of infected agents or those describing the network's

topology, associated significantly with measured atrophy (Fig. 5). As for gene expression, the deformation-based morphometry-derived tissue deformation was associated with neither *SNCA* ( $r=0.24$ ,  $p=0.12$ ) nor *GBA* ( $r=0.18$ ,  $p=0.24$ ) regional expression. This demonstrates that brain connectivity or gene expression alone cannot predict atrophy in iRBD, and that the full agent-based SIR model taking into account gene expression, connectivity, and deafferentation provides the best fit to the measured deformation.

### **Connectivity and gene expression shape alpha-synuclein spread.**

We further investigated the importance of connectome architecture and gene expression by generating several null models. The peak fits of the SIR model were compared to the peak fits observed in null distributions derived from simulations where either gene expression or network architecture were randomly shuffled across regions. We observed that randomizing *SNCA* and *GBA* expression levels (i.e., alpha-synuclein synthesis and clearance) significantly disrupted the model fit at a 40% connection density; however, randomizing the *SNCA* expression did not disrupt the fit at lower connection densities (Fig. 6). The randomization of connectivity was performed using two different types of null models to assess the impact of network topology and/or geometry on alpha-synuclein spread. In both cases, randomizing the connectome's architecture disrupted the model fit (Fig. 6), indicating that both the brain's structural connectivity pattern and the physical constraints imposed on the connectome contribute to shaping atrophy. Taken together, this demonstrates that connectivity and gene expression combine to shape brain atrophy of iRBD.

## **Discussion**

Isolated RBD is associated with brain volume and cortical thickness atrophy.<sup>6-8,56-61</sup> Patients also present with high rates of positivity to pathologic alpha-synuclein in tissue biopsies.<sup>62-65</sup> However, a mechanistic understanding of how alpha-synuclein pathology may relate to the patterns of brain atrophy in iRBD remains unknown. Here, we quantified atrophy in the largest multicentric cohort of polysomnography-confirmed iRBD patients

with T1-weighted MRI acquired to date and applied the agent-based SIR model to test whether prion-like and regional vulnerability factors recreated the atrophy in iRBD. We demonstrated that the computational simulation of atrophy based on the connectome's architecture and gene expression of *SNCA* and *GBA* did recreate the atrophy seen in iRBD patients. Since most of the atrophy in iRBD associates with cognitive impairment,<sup>7</sup> and given that atrophy predicts dementia with Lewy bodies in iRBD,<sup>8</sup> this study sheds light on the specific mechanisms underlying the development of dementia with Lewy bodies in this population.

The agent-based SIR model simulates the spread of alpha-synuclein based on brain connectivity and the expression of genes involved in alpha-synuclein synthesis and clearance.<sup>21</sup> This model recreates the atrophy seen in Parkinson's disease<sup>21</sup> and frontotemporal dementia,<sup>47</sup> and the spatiotemporal patterns of pathologic alpha-synuclein quantified in non-transgenic mice injected with preformed fibrils into either the striatum, nucleus accumbens or hippocampus.<sup>22</sup> In the current work, we show that the atrophy in iRBD also follows the constraints imposed by the connectome's architecture and the gene expression of *SNCA* and *GBA*. The impact of these factors was decisive, as demonstrated by the model's inability to recreate atrophy if either connectivity or gene expression were randomized. The influence of connectivity is in line with several studies showing that cerebral connectivity forecasts the atrophy seen in neurodegenerative diseases,<sup>66-68</sup> including Parkinson's disease.<sup>20,21</sup> The influence of *SNCA* and *GBA* gene expression also agrees with mutations in these genes being significant risk factors for Parkinson's disease and dementia with Lewy bodies.<sup>69-71</sup> We observed that, whereas randomizing *GBA* expression always interfered with the model's ability to recreate atrophy, the randomization of *SNCA* expression only led to a disruption at the 40% connection density, suggesting that *GBA* expression exerts an effect on the spread (and hence atrophy) that is more consistent than *SNCA*. The reason for this difference is unclear but does not seem related to different gene expression levels used by the model (*SNCA*:  $0.17 \pm 0.66$  (range: 2.91) versus *GBA*:  $0.03 \pm 0.51$  (range: 2.95),  $p=0.28$ ). Another possibility is that the 90 additional connections appearing in the 40% density connectome were particularly

influential for *SNCA* to exert its effect on atrophy. Further studies should therefore investigate more closely the effect of gene expression on atrophy in iRBD. Nonetheless, this is consistent with our previous work showing that atrophy in Parkinson's disease is shaped by local concentration of alpha-synuclein and connectivity, supporting the prion model.<sup>21</sup>

However, although the model recreated atrophy, the visual inspection of observed and simulated atrophy measurements at the peak fit showed some inconsistencies. For instance, while the middle temporal gyrus was the region showing the greatest tissue deformation in iRBD, the amount of simulated atrophy was modest. This could suggest that proteins other than alpha-synuclein, disease-related changes in connectivity, regional vulnerability to alpha-synuclein accumulation unaccounted for in the model, and/or other mechanistic explanations may be involved in the observed changes in the middle temporal gyrus. However, in contrast, neighbouring regions such as the amygdala and the entorhinal cortex, which were reported to show high burden of Lewy pathology in brains of Lewy body patients,<sup>72</sup> were also among the regions showing the highest amount of simulated atrophy in our patterns.

Another novelty of this study is the comprehensive assessment of brain morphology in a large multicentric cohort of iRBD patients with polysomnography and T1-weighted MRI acquisition. We found that iRBD patients had volume atrophy in the middle temporal gyrus and cortical thinning in the frontal, posterior temporal, occipital, and inferior parietal cortices, which is in line with earlier findings in smaller iRBD cohorts.<sup>28</sup> Morphological changes related to clinical changes, with the severity of parkinsonism being associated with extensive cortical thinning, thickening of the sensorimotor cortex, and increased area in posterior regions. Whereas the paracentral, sensorimotor, and superior parietal areas have been associated with motor deficits in iRBD,<sup>6,59</sup> other regions such as the frontal and temporal cortices were not expected to be involved based on previous work. However, this frontotemporal pattern has already been documented in Parkinson's disease<sup>73</sup> and our findings here may represent premorbid neurodegenerative changes typical of overt

Parkinson's disease. As for the MoCA correlates, the pattern was in line with what was previously observed for global cognitive performance in Parkinson's disease<sup>73</sup> and included the anterior insula, which was shown to be particularly vulnerable in synucleinopathies affecting cognition.<sup>74-77</sup>

This study has some limitations. First, the brainstem nuclei involved in REM sleep motor atonia<sup>78</sup> were not included in our analyses. This is due to the difficulty in imaging both brain atrophy and connectivity in these structures. Second, scans were acquired using different acquisition parameters at different sites. In the current work, site effects were regressed out from atrophy measurements during *W*-scoring and entered as covariate in neuroimaging analyses. The use of harmonized *W*-scores using a batch-correcting tool validated for neuroimaging data yielded the same results. Third, alpha-synuclein spread was simulated on a healthy structural connectome and transcriptome. White matter abnormalities and topological disorganization of grey matter have been reported in iRBD,<sup>8,58,79,80</sup> as well as a genetic makeup more complex than the sole effects of *SNCA* and *GBA*.<sup>81</sup> Once these changes are more thoroughly understood in iRBD, they can be implemented in the model.

In summary, atrophy in iRBD patients can be recreated using a combination of agent-based modelling, structural connectomics, and gene expression. The agent-based SIR model may provide a way to test new research hypotheses for the purpose of slowing or stopping the spread of pathologic alpha-synuclein in the brain.

## Acknowledgements

Shady Rahayel reports a scholarship from the Fonds de recherche du Québec – Santé. Jean-François Gagnon holds a Canada Research Chair in Cognitive Decline in Pathological Aging. Kaylena Ehgoetz Martens reports a scholarship from Parkinson Canada and Sydney Fellowship. Data used in this article included data from the Parkinson's Progression

Markers Initiative database (<https://www.ppmi-info.org>), a public-private partnership, funded by the Michael J. Fox Foundation for Parkinson's Research.

## Funding

The ICEBERG Study performed in Paris was funded by the “Investissements d’Avenir”, IAIHU-06 (Paris Institute of Neurosciences – IHU), ANR-11-INBS-0006, Fondation d’Entreprise EDF, Biogen Inc., Fondation Thérèse and René Planiol, unrestricted support for research on Parkinson's disease from Energipole (M. Mallart) and Société Française de Médecine Esthétique (M. Legrand). The work was also supported by a grant from Institut de France to Isabelle Arnulf (Alice Study) and received funding from the program “Investissements d’Avenir” (ANR-10-IAIHU-06).

The work performed in Montreal was supported by the Canadian Institutes of Health Research, the Fonds de recherche du Québec – Santé, and the W. Garfield Weston Foundation. Jean-François Gagnon reports grants from the Fonds de recherche du Québec – Santé, the Canadian Institutes of Health Research, the W. Garfield Weston Foundation, the Michael J. Fox Foundation, and the National Institutes of Health. Ronald B. Postuma reports grants and personal fees from the Fonds de recherche du Québec – Santé, the Canadian Institutes of Health Research, The Parkinson Society of Canada, the W. Garfield Weston Foundation, the Michael J. Fox Foundation, the Webster Foundation, and the National Institutes of Health. This work was also funded by awards from the Canadian Institutes of Health Research Foundation Scheme and the Healthy Brains for Healthy Lives initiative to Alain Dagher.

The work performed in Sydney was supported by an NHMRC Dementia Team Grant (#1095127). Simon Lewis is supported by an NHMRC Leadership Fellowship (#1195830). Elie Matar reports funding from the National Health and Medical Research Council, grant 2008565.

The work performed in Aarhus was supported by funding from the Lundbeck Foundation, the Danish Parkinson's Disease Association, and the Jascha Foundation.

## Competing interests

Shady Rahayel, Christina Tremblay, Andrew Vo, Ying-Qiu Zheng, Stéphane Lehericy, Marie Vidailhet, Jean-François Gagnon, Jacques Montplaisir, Simon Lewis, Elie Matar, Kaylena Ehgoetz Martens, Per Borghammer, Karoline Knudsen, Allan Hansen, Oury Monchi, Bratislav Misic, and Alain Dagher report no competing interests.

Isabelle Arnulf reports consultancies with Idorsia Pharma and paid speaker bureau for UCB Pharma, unrelated to the study. Jean-Christophe Corvol reports fees for advisory boards for Biogen, Denali, Idorsia, Prevail Therapeutic, Theranexus, UCB, and grants from Sanofi and the Michael J. Fox Foundation, outside the current work. Ronald B. Postuma reports grants and personal fees from Roche, personal fees from Takeda, Teva Neurosciences, Biogen, Boehringer Ingelheim, Theranexus, GE HealthCare, Jazz Pharmaceuticals, Abbvie, Janssen, Otsuko, Phytopharmics, Inception Sciences, and Paladin outside the submitted work.

## Appendix 1

List of the contributors involved in the ICEBERG Study Group:

Steering committee: Marie Vidailhet, MD, PhD, (Pitié-Salpêtrière Hospital, Paris, principal investigator of ICEBERG), Jean-Christophe Corvol, MD, PhD (Pitié-Salpêtrière Hospital, Paris, scientific lead), Isabelle Arnulf, MD, PhD (Pitié-Salpêtrière Hospital, Paris, member of the steering committee), Stéphane Lehericy, MD, PhD (Pitié-Salpêtrière Hospital, Paris, member of the steering committee);

Clinical data: Marie Vidailhet, MD, PhD, (Pitié-Salpêtrière Hospital, Paris, coordination), Graziella Mangone, MD, PhD (Pitié-Salpêtrière Hospital, Paris, co-coordination), Jean-Christophe Corvol, MD, PhD (Pitié-Salpêtrière Hospital, Paris), Isabelle Arnulf, MD, PhD (Pitié-Salpêtrière Hospital, Paris), Sara Sambin, MD (Pitié-Salpêtrière Hospital, Paris), Jonas Ihle, MD (Pitié-Salpêtrière Hospital, Paris), Caroline Weill, MD, (Pitié-Salpêtrière Hospital, Paris), David Grabli, MD, PhD (Pitié-Salpêtrière Hospital, Paris); Florence Cormier-Dequaire, MD (Pitié-Salpêtrière Hospital, Paris); Louise Laure Mariani, MD,

PhD (Pitié-Salpêtrière Hospital, Paris), Bertrand Degos, MD, PhD (Avicenne Hospital, Bobigny);

Neuropsychological data: Richard Levy, MD (Pitié-Salpêtrière Hospital, Paris, coordination), Fanny Pineau, MS (Pitié-Salpêtrière Hospital, Paris, neuropsychologist), Julie Socha, MS (Pitié-Salpêtrière Hospital, Paris, neuropsychologist), Eve Benchetrit, MS (La Timone Hospital, Marseille, neuropsychologist), Virginie Czernecki, MS (Pitié-Salpêtrière Hospital, Paris, neuropsychologist), Marie-Alexandrine, MS (Pitié-Salpêtrière Hospital, Paris, neuropsychologist);

Eye movement: Sophie Rivaud-Pechoux, PhD (ICM, Paris, coordination); Elodie Hainque, MD, PhD (Pitié-Salpêtrière Hospital, Paris);

Sleep assessment: Isabelle Arnulf, MD, PhD (Pitié-Salpêtrière Hospital, Paris, coordination), Smaranda Leu Semenescu, MD (Pitié-Salpêtrière Hospital, Paris), Pauline Dodet, MD (Pitié-Salpêtrière Hospital, Paris);

Genetic data: Jean-Christophe Corvol, MD, PhD (Pitié-Salpêtrière Hospital, Paris, coordination), Graziella Mangone, MD, PhD (Pitié-Salpêtrière Hospital, Paris, co-coordination), Samir Bekadar, MS (Pitié-Salpêtrière Hospital, Paris, biostatistician), Alexis Brice, MD (ICM, Pitié-Salpêtrière Hospital, Paris), Suzanne Lesage, PhD (INSERM, ICM, Paris, genetic analyses);

Metabolomics: Fanny Mochel, MD, PhD (Pitié-Salpêtrière Hospital, Paris, coordination), Farid Ichou, PhD (ICAN, Pitié-Salpêtrière Hospital, Paris), Vincent Perlberg, PhD, Pierre and Marie Curie University), Benoit Colsch, PhD (CEA, Saclay), Arthur Tenenhaus, PhD (Supelec, Gif-sur-Yvette, data integration);

Brain MRI data: Stéphane Lehericy, MD, PhD (Pitié-Salpêtrière Hospital, Paris, coordination), Rahul Gaurav, MS, (Pitié-Salpêtrière Hospital, Paris, data analysis), Nadya Pyatigorskaya, MD, PhD, (Pitié-Salpêtrière Hospital, Paris, data analysis); Lydia Yahia-Cherif, PhD (ICM, Paris, Biostatistics), Romain Valabregue, PhD (ICM, Paris, data analysis), Cécile Galléa, PhD (ICM, Paris);

Datscan imaging data: Marie-Odile Habert, MCU-PH (Pitié-Salpêtrière Hospital, Paris, coordination);

Voice recording: Dijana Petrovska, PhD (Telecom Sud Paris, Evry, coordination), Laetitia Jeancolas, MS (Telecom Sud Paris, Evry);

Study management: Vanessa Brochard (Pitié-Salpêtrière Hospital, Paris, coordination), Alizé Chalançon (Pitié-Salpêtrière Hospital, Paris, Project manager), Carole Dongmo-Kenfack (Pitié-Salpêtrière Hospital, Paris, clinical research assistant); Christelle Laganot (Pitié-Salpêtrière Hospital, Paris, clinical research assistant), Valentine Maheo (Pitié-Salpêtrière Hospital, Paris, clinical research assistant).

## References

1. Hogl B, Stefani A, Videnovic A. Idiopathic REM sleep behaviour disorder and neurodegeneration - an update. *Nat Rev Neurol*. Jan 2018;14(1):40-55. doi:10.1038/nrneurol.2017.157
2. Miglis MG, Adler CH, Antelmi E, et al. Biomarkers of conversion to alpha-synucleinopathy in isolated rapid-eye-movement sleep behaviour disorder. *Lancet Neurol*. Aug 2021;20(8):671-684. doi:10.1016/S1474-4422(21)00176-9
3. Postuma RB, Iranzo A, Hu M, et al. Risk and predictors of dementia and parkinsonism in idiopathic REM sleep behaviour disorder: a multicentre study. *Brain*. Mar 1 2019;142(3):744-759. doi:10.1093/brain/awz030
4. Shen Y, Yu WB, Shen B, et al. Propagated alpha-synucleinopathy recapitulates REM sleep behaviour disorder followed by parkinsonian phenotypes in mice. *Brain*. Dec 5 2020;143(11):3374-3392. doi:10.1093/brain/awaa283
5. McKenna D, Peever J. Degeneration of rapid eye movement sleep circuitry underlies rapid eye movement sleep behavior disorder. *Mov Disord*. May 2017;32(5):636-644. doi:10.1002/mds.27003

6. Rahayel S, Postuma RB, Montplaisir J, et al. Abnormal Gray Matter Shape, Thickness, and Volume in the Motor Cortico-Subcortical Loop in Idiopathic Rapid Eye Movement Sleep Behavior Disorder: Association with Clinical and Motor Features. *Cereb Cortex*. Feb 1 2018;28(2):658-671. doi:10.1093/cercor/bhx137
7. Rahayel S, Postuma RB, Montplaisir J, et al. Cortical and subcortical gray matter bases of cognitive deficits in REM sleep behavior disorder. *Neurology*. May 15 2018;90(20):e1759-e1770. doi:10.1212/WNL.0000000000005523
8. Rahayel S, Postuma RB, Montplaisir J, et al. A Prodromal Brain-Clinical Pattern of Cognition in Synucleinopathies. *Ann Neurol*. Feb 2021;89(2):341-357. doi:10.1002/ana.25962
9. Guo YJ, Xiong H, Chen K, Zou JJ, Lei P. Brain regions susceptible to alpha-synuclein spreading. *Mol Psychiatry*. Sep 24 2021;doi:10.1038/s41380-021-01296-7
10. Braak H, Del Tredici K, Rub U, de Vos RA, Jansen Steur EN, Braak E. Staging of brain pathology related to sporadic Parkinson's disease. *Neurobiol Aging*. Mar-Apr 2003;24(2):197-211.
11. Braak H, Ghebremedhin E, Rub U, Bratzke H, Del Tredici K. Stages in the development of Parkinson's disease-related pathology. *Cell Tissue Res*. Oct 2004;318(1):121-34. doi:10.1007/s00441-004-0956-9
12. Rey NL, George S, Steiner JA, et al. Spread of aggregates after olfactory bulb injection of alpha-synuclein fibrils is associated with early neuronal loss and is reduced long term. *Acta Neuropathol*. Jan 2018;135(1):65-83. doi:10.1007/s00401-017-1792-9
13. Rey NL, Steiner JA, Maroof N, et al. Widespread transneuronal propagation of alpha-synucleinopathy triggered in olfactory bulb mimics prodromal Parkinson's disease. *J Exp Med*. Aug 22 2016;213(9):1759-78. doi:10.1084/jem.20160368
14. Luk KC, Kehm V, Carroll J, et al. Pathological alpha-synuclein transmission initiates Parkinson-like neurodegeneration in nontransgenic mice. *Science*. Nov 16 2012;338(6109):949-53. doi:10.1126/science.1227157

15. Luk KC, Kehm VM, Zhang B, O'Brien P, Trojanowski JQ, Lee VM. Intracerebral inoculation of pathological alpha-synuclein initiates a rapidly progressive neurodegenerative alpha-synucleinopathy in mice. *J Exp Med*. May 7 2012;209(5):975-86. doi:10.1084/jem.20112457
16. Masuda-Suzukake M, Nonaka T, Hosokawa M, et al. Prion-like spreading of pathological alpha-synuclein in brain. *Brain*. Apr 2013;136(Pt 4):1128-38. doi:10.1093/brain/awt037
17. Van Den Berge N, Ferreira N, Gram H, et al. Evidence for bidirectional and trans-synaptic parasympathetic and sympathetic propagation of alpha-synuclein in rats. *Acta Neuropathol*. Oct 2019;138(4):535-550. doi:10.1007/s00401-019-02040-w
18. Zeighami Y, Ulla M, Iturria-Medina Y, et al. Network structure of brain atrophy in de novo Parkinson's disease. *Elife*. Sep 7 2015;4doi:10.7554/eLife.08440
19. Yau Y, Zeighami Y, Baker TE, et al. Network connectivity determines cortical thinning in early Parkinson's disease progression. *Nat Commun*. Jan 2 2018;9(1):12. doi:10.1038/s41467-017-02416-0
20. Tremblay C, Rahayel S, Vo A, et al. Brain atrophy progression in Parkinson's disease is shaped by connectivity and local vulnerability. *Brain Commun*. 2021;3(4):fcab269. doi:10.1093/braincomms/fcab269
21. Zheng YQ, Zhang Y, Yau Y, et al. Local vulnerability and global connectivity jointly shape neurodegenerative disease propagation. *PLoS Biol*. Nov 2019;17(11):e3000495. doi:10.1371/journal.pbio.3000495
22. Rahayel S, Misic B, Zheng YQ, et al. Differentially targeted seeding reveals unique pathologic alpha-synuclein propagation patterns. *Brain*. 2021;
23. Marek K, Chowdhury S, Siderowf A, et al. The Parkinson's progression markers initiative (PPMI) - establishing a PD biomarker cohort. *Ann Clin Transl Neurol*. Dec 2018;5(12):1460-1477. doi:10.1002/acn3.644
24. Postuma RB, Berg D, Stern M, et al. MDS clinical diagnostic criteria for Parkinson's disease. *Mov Disord*. Oct 2015;30(12):1591-601. doi:10.1002/mds.26424

25. McKeith IG, Boeve BF, Dickson DW, et al. Diagnosis and management of dementia with Lewy bodies: Fourth consensus report of the DLB Consortium. *Neurology*. Jul 4 2017;89(1):88-100. doi:10.1212/WNL.0000000000004058
26. Ashburner J, Hutton C, Frackowiak R, Johnsrude I, Price C, Friston K. Identifying global anatomical differences: deformation-based morphometry. *Hum Brain Mapp*. 1998;6(5-6):348-57.
27. Ashburner J, Friston KJ. Unified segmentation. *Neuroimage*. Jul 1 2005;26(3):839-51. doi:10.1016/j.neuroimage.2005.02.018
28. Campabadal A, Segura B, Junque C, Iranzo A. Structural and functional magnetic resonance imaging in isolated REM sleep behavior disorder: A systematic review of studies using neuroimaging software. *Sleep Med Rev*. Apr 22 2021;59:101495. doi:10.1016/j.smrv.2021.101495
29. Reuter M, Schmansky NJ, Rosas HD, Fischl B. Within-subject template estimation for unbiased longitudinal image analysis. *Neuroimage*. Jul 16 2012;61(4):1402-18. doi:10.1016/j.neuroimage.2012.02.084
30. Dale AM, Fischl B, Sereno MI. Cortical surface-based analysis. I. Segmentation and surface reconstruction. *Neuroimage*. Feb 1999;9(2):179-94. doi:10.1006/nimg.1998.0395
31. Klapwijk ET, van de Kamp F, van der Meulen M, Peters S, Wierenga LM. Qoala-T: A supervised-learning tool for quality control of FreeSurfer segmented MRI data. *Neuroimage*. Apr 1 2019;189:116-129. doi:10.1016/j.neuroimage.2019.01.014
32. Monereo-Sanchez J, de Jong JJA, Drenthen GS, et al. Quality control strategies for brain MRI segmentation and parcellation: Practical approaches and recommendations - insights from the Maastricht study. *Neuroimage*. Aug 15 2021;237:118174. doi:10.1016/j.neuroimage.2021.118174
33. Tremblay C, Abbasi N, Zeighami Y, et al. Sex effects on brain structure in de novo Parkinson's disease: a multimodal neuroimaging study. *Brain*. Oct 1 2020;143(10):3052-3066. doi:10.1093/brain/awaa234

34. Desikan RS, Segonne F, Fischl B, et al. An automated labeling system for subdividing the human cerebral cortex on MRI scans into gyral based regions of interest. *Neuroimage*. Jul 01 2006;31(3):968-80. doi:10.1016/j.neuroimage.2006.01.021
35. Fischl B, Salat DH, Busa E, et al. Whole brain segmentation: automated labeling of neuroanatomical structures in the human brain. *Neuron*. Jan 31 2002;33(3):341-55.
36. Biondetti E, Santin MD, Valabregue R, et al. The spatiotemporal changes in dopamine, neuromelanin and iron characterizing Parkinson's disease. *Brain*. May 12 2021;doi:10.1093/brain/awab191
37. Barber TR, Griffanti L, Bradley KM, et al. Nigrosome 1 imaging in REM sleep behavior disorder and its association with dopaminergic decline. *Ann Clin Transl Neurol*. Jan 2020;7(1):26-35. doi:10.1002/acn3.50962
38. Keuken MC, Bazin PL, Crown L, et al. Quantifying inter-individual anatomical variability in the subcortex using 7 T structural MRI. *Neuroimage*. Jul 1 2014;94:40-46. doi:10.1016/j.neuroimage.2014.03.032
39. Hawrylycz MJ, Lein ES, Guillozet-Bongaarts AL, et al. An anatomically comprehensive atlas of the adult human brain transcriptome. *Nature*. Sep 20 2012;489(7416):391-399. doi:10.1038/nature11405
40. Yeh CH, Jones DK, Liang X, Descoteaux M, Connelly A. Mapping Structural Connectivity Using Diffusion MRI: Challenges and Opportunities. *J Magn Reson Imaging*. Jun 2021;53(6):1666-1682. doi:10.1002/jmri.27188
41. Maier-Hein KH, Neher PF, Houde JC, et al. The challenge of mapping the human connectome based on diffusion tractography. *Nat Commun*. Nov 7 2017;8(1):1349. doi:10.1038/s41467-017-01285-x
42. Barnes J, Ridgway GR, Bartlett J, et al. Head size, age and gender adjustment in MRI studies: a necessary nuisance? *Neuroimage*. Dec 2010;53(4):1244-55. doi:10.1016/j.neuroimage.2010.06.025

43. Winkler AM, Kochunov P, Blangero J, et al. Cortical thickness or grey matter volume? The importance of selecting the phenotype for imaging genetics studies. *Neuroimage*. Nov 15 2010;53(3):1135-46. doi:10.1016/j.neuroimage.2009.12.028
44. Fortin JP, Cullen N, Sheline YI, et al. Harmonization of cortical thickness measurements across scanners and sites. *Neuroimage*. Feb 15 2018;167:104-120. doi:10.1016/j.neuroimage.2017.11.024
45. Fortin JP, Parker D, Tunc B, et al. Harmonization of multi-site diffusion tensor imaging data. *Neuroimage*. Nov 1 2017;161:149-170. doi:10.1016/j.neuroimage.2017.08.047
46. Johnson WE, Li C, Rabinovic A. Adjusting batch effects in microarray expression data using empirical Bayes methods. *Biostatistics*. Jan 2007;8(1):118-27. doi:10.1093/biostatistics/kxj037
47. Shafiei G, Bazinet V, Dadar M, et al. Global network structure and local transcriptomic vulnerability shape atrophy in sporadic and genetic behavioral variant frontotemporal dementia. *bioRxiv*. 2021:2021.08.24.457538. doi:10.1101/2021.08.24.457538
48. Betzel RF, Griffa A, Hagmann P, Misic B. Distance-dependent consensus thresholds for generating group-representative structural brain networks. *Netw Neurosci*. 2019;3(2):475-496. doi:10.1162/netn\_a\_00075
49. Misic B, Betzel RF, Griffa A, et al. Network-Based Asymmetry of the Human Auditory System. *Cereb Cortex*. Jul 1 2018;28(7):2655-2664. doi:10.1093/cercor/bhy101
50. Misic B, Betzel RF, Nematzadeh A, et al. Cooperative and Competitive Spreading Dynamics on the Human Connectome. *Neuron*. Jun 17 2015;86(6):1518-29. doi:10.1016/j.neuron.2015.05.035
51. Markello RD, Shafiei G, Zheng YQ, Misic B. abagen: A toolbox for the Allen Brain Atlas genetics data. *Zenodo*. 2020;https://doi.org/10.5281.zenodo.372

52. Benjamini Y, Drai D, Elmer G, Kafkafi N, Golani I. Controlling the false discovery rate in behavior genetics research. *Behav Brain Res*. Nov 1 2001;125(1-2):279-84. doi:10.1016/s0166-4328(01)00297-2
53. Mowinckel AM, Vidal-Piñeiro D. Visualization of Brain Statistics With R Packages ggseg and ggseg3d. *Advances in Methods and Practices in Psychological Science*. 2020/12/01 2020;3(4):466-483. doi:10.1177/2515245920928009
54. Rubinov M, Sporns O. Complex network measures of brain connectivity: uses and interpretations. *Neuroimage*. Sep 2010;52(3):1059-69. doi:10.1016/j.neuroimage.2009.10.003
55. Maslov S, Sneppen K. Specificity and stability in topology of protein networks. *Science*. May 3 2002;296(5569):910-3. doi:10.1126/science.1065103
56. Rahayel S, Montplaisir J, Monchi O, et al. Patterns of cortical thinning in idiopathic rapid eye movement sleep behavior disorder. *Mov Disord*. Apr 15 2015;30(5):680-7. doi:10.1002/mds.25820
57. Campabadal A, Inguanzo A, Segura B, et al. Cortical gray matter progression in idiopathic REM sleep behavior disorder and its relation to cognitive decline. *Neuroimage Clin*. 2020;28:102421. doi:10.1016/j.nicl.2020.102421
58. Holtbernd F, Romanzetti S, Oertel WH, et al. Convergent patterns of structural brain changes in rapid eye movement sleep behavior disorder and Parkinson's disease on behalf of the German rapid eye movement sleep behavior disorder study group. *Sleep*. Mar 12 2021;44(3)doi:10.1093/sleep/zsaa199
59. Pereira JB, Weintraub D, Chahine L, Aarsland D, Hansson O, Westman E. Cortical thinning in patients with REM sleep behavior disorder is associated with clinical progression. *NPJ Parkinsons Dis*. 2019;5:7. doi:10.1038/s41531-019-0079-3
60. Scherfler C, Frauscher B, Schocke M, et al. White and gray matter abnormalities in idiopathic rapid eye movement sleep behavior disorder: a diffusion-tensor imaging and voxel-based morphometry study. *Ann Neurol*. Feb 2011;69(2):400-7. doi:10.1002/ana.22245

61. Hanyu H, Inoue Y, Sakurai H, et al. Voxel-based magnetic resonance imaging study of structural brain changes in patients with idiopathic REM sleep behavior disorder. *Parkinsonism Relat Disord*. Feb 2012;18(2):136-9. doi:10.1016/j.parkreldis.2011.08.023
62. Al-Qassabi A, Tsao TS, Racolta A, et al. Immunohistochemical Detection of Synuclein Pathology in Skin in Idiopathic Rapid Eye Movement Sleep Behavior Disorder and Parkinsonism. *Mov Disord*. Apr 2021;36(4):895-904. doi:10.1002/mds.28399
63. Stefani A, Iranzo A, Holzknecht E, et al. Alpha-synuclein seeds in olfactory mucosa of patients with isolated REM sleep behaviour disorder. *Brain*. May 7 2021;144(4):1118-1126. doi:10.1093/brain/awab005
64. Antelmi E, Donadio V, Incensi A, Plazzi G, Liguori R. Skin nerve phosphorylated alpha-synuclein deposits in idiopathic REM sleep behavior disorder. *Neurology*. May 30 2017;88(22):2128-2131. doi:10.1212/WNL.0000000000003989
65. Doppler K, Jentschke HM, Schulmeyer L, et al. Dermal phospho-alpha-synuclein deposits confirm REM sleep behaviour disorder as prodromal Parkinson's disease. *Acta Neuropathol*. Apr 2017;133(4):535-545. doi:10.1007/s00401-017-1684-z
66. Zhou J, Gennatas ED, Kramer JH, Miller BL, Seeley WW. Predicting regional neurodegeneration from the healthy brain functional connectome. *Neuron*. Mar 22 2012;73(6):1216-27. doi:10.1016/j.neuron.2012.03.004
67. Tetreault AM, Phan T, Orlando D, et al. Network localization of clinical, cognitive, and neuropsychiatric symptoms in Alzheimer's disease. *Brain*. Apr 1 2020;143(4):1249-1260. doi:10.1093/brain/awaa058
68. Brown JA, Deng J, Neuhaus J, et al. Patient-Tailored, Connectivity-Based Forecasts of Spreading Brain Atrophy. *Neuron*. Dec 4 2019;104(5):856-868 e5. doi:10.1016/j.neuron.2019.08.037
69. Krohn L, Wu RYJ, Heilbron K, et al. Fine-Mapping of SNCA in Rapid Eye Movement Sleep Behavior Disorder and Overt Synucleinopathies. *Ann Neurol*. Apr 2020;87(4):584-598. doi:10.1002/ana.25687

70. Avenali M, Blandini F, Cerri S. Glucocerebrosidase Defects as a Major Risk Factor for Parkinson's Disease. *Front Aging Neurosci.* 2020;12:97. doi:10.3389/fnagi.2020.00097
71. Chia R, Sabir MS, Bandres-Ciga S, et al. Genome sequencing analysis identifies new loci associated with Lewy body dementia and provides insights into its genetic architecture. *Nat Genet.* Mar 2021;53(3):294-303. doi:10.1038/s41588-021-00785-3
72. Raunio A, Kaivola K, Tuimala J, et al. Lewy-related pathology exhibits two anatomically and genetically distinct progression patterns: a population-based study of Finns aged 85. *Acta Neuropathol.* Nov 2019;138(5):771-782. doi:10.1007/s00401-019-02071-3
73. Wilson H, Niccolini F, Pellicano C, Politis M. Cortical thinning across Parkinson's disease stages and clinical correlates. *J Neurol Sci.* Mar 15 2019;398:31-38. doi:10.1016/j.jns.2019.01.020
74. Blanc F, Colloby SJ, Philippi N, et al. Cortical Thickness in Dementia with Lewy Bodies and Alzheimer's Disease: A Comparison of Prodromal and Dementia Stages. *PLoS One.* 2015;10(6):e0127396. doi:10.1371/journal.pone.0127396
75. Roquet D, Noblet V, Anthony P, et al. Insular atrophy at the prodromal stage of dementia with Lewy bodies: a VBM DARTEL study. *Sci Rep.* Aug 25 2017;7(1):9437. doi:10.1038/s41598-017-08667-7
76. Zhong J, Pan P, Dai Z, Shi H. Voxelwise meta-analysis of gray matter abnormalities in dementia with Lewy bodies. *Eur J Radiol.* Oct 2014;83(10):1870-4. doi:10.1016/j.ejrad.2014.06.014
77. Fathy YY, Jonker AJ, Oudejans E, et al. Differential insular cortex subregional vulnerability to alpha-synuclein pathology in Parkinson's disease and dementia with Lewy bodies. *Neuropathol Appl Neurobiol.* Apr 2019;45(3):262-277. doi:10.1111/nan.12501
78. Wang YQ, Liu WY, Li L, Qu WM, Huang ZL. Neural circuitry underlying REM sleep: A review of the literature and current concepts. *Prog Neurobiol.* Sep 2021;204:102106. doi:10.1016/j.pneurobio.2021.102106

79. Unger MM, Belke M, Menzler K, et al. Diffusion tensor imaging in idiopathic REM sleep behavior disorder reveals microstructural changes in the brainstem, substantia nigra, olfactory region, and other brain regions. *Sleep*. Jun 2010;33(6):767-73.
80. Park KM, Lee HJ, Lee BI, Kim SE. Alterations of the brain network in idiopathic rapid eye movement sleep behavior disorder: structural connectivity analysis. *Sleep Breath*. Jun 2019;23(2):587-593. doi:10.1007/s11325-018-1737-0
81. Krohn L, Heilbron K, Blauwendraat C, et al. Genome-wide association study of REM sleep behavior disorder identifies novel loci with distinct polygenic and brain expression effects. *medRxiv*. 2021:2021.09.08.21254232. doi:10.1101/2021.09.08.21254232
82. Fahn S, Elton R, Members of the UPDRS Development Committee. Unified Parkinson's Disease Rating Scale. In: Fahn S, Marsden CD, Calne DB, Goldstein M, eds.

## Tables

**Table 1 Demographics and clinical variables of iRBD patients and controls.**

Variables	iRBD (n=171)	Controls (n=238)	p-value
Age, years	67.7 ± 6.6 (49-87)	66.6 ± 7.9 (41-88)	0.112 <sup>a</sup>
Sex, n (% men)	142 (83%)	183 (77%)	0.129 <sup>b</sup>
MDS-UPDRS-III <sup>c</sup>	7.4 ± 6.9 (0-34)	2.3 ± 3.7 (0-19)	<0.001 <sup>d</sup>
UPDRS-III (Fahn & Elton) <sup>e</sup>	4.3 ± 3.6 (0-19)	-	-
MoCA	26.3 ± 3.1 (11-30)	27.9 ± 1.7 (20-30)	<0.001 <sup>d</sup>

Continuous data are presented as mean ± SD (range).

<sup>a</sup>Student's t test.

<sup>b</sup>Chi-squared test.

<sup>c</sup>Available in 123 patients and 154 controls.

<sup>d</sup>Mann-Whitney U test.

<sup>e</sup>The Montreal cohort underwent the Fahn & Elton UPDRS-III version.<sup>82</sup>

CI = confidence interval; iRBD = isolated REM sleep behaviour disorder; MDS = Movement Disorders Society; MoCA = Montreal Cognitive Assessment; UPDRS-III = Unified Parkinson's Disease Rating Scale, motor examination.

**Table 2 Results of vertex-based cortical analyses between iRBD patients and controls.**

Cortical measure	Most affected regions	Hemi-sphere	Cluster size, mm <sup>2</sup>	Number of vertices	Talairach coordinates			-log <sub>10</sub> p-value
					x	y	z	
Between group comparisons								
Thickness <sup>a</sup>	Cluster: Inferior parietal and lateral occipital	Right	5,740.0	9,280	41.8	-70.0	23.0	4.332
	Cluster: Rostral and caudal middle frontal, superior frontal, medial orbitofrontal, pars orbitalis	Left	6,470.4	10,938	-33.6	35.6	23.9	2.652
	Cluster: Inferior parietal, inferior, middle, superior temporal cortex	Left	4,766.7	8,943	-38.2	-52.8	22.5	2.306
Surface area <sup>b</sup>	Cluster: Inferior temporal and entorhinal	Left	2,615.5	4,458	-50.1	-45.3	-14.0	-2.983
MDS-UPDRS-III: Correlation analysis in iRBD								
Thickness	Cluster: Inferior, middle, and superior temporal <sup>c</sup>	Right	3751.0	6,712	54.9	-25.0	-18.1	-4.295
	Cluster: Superior frontal, pars opercularis, triangularis, orbitalis, rostral and caudal middle frontal, medial and lateral orbitofrontal, precentral and postcentral <sup>c</sup>	Left	14557.5	26,102	-7.2	36.9	-20.6	-4.043
	Cluster: Medial and lateral orbitofrontal, pars opercularis, triangularis, orbitalis <sup>c</sup>	Right	5389.5	8,843	6.7	51.5	-17.8	-3.987
	Cluster: Superior frontal, rostral and caudal middle frontal <sup>c</sup>	Right	5061.7	9,439	9.0	38.2	28.3	-3.879
	Cluster: Precentral and postcentral <sup>d</sup>	Right	2205.7	5,010	8.3	-25.8	63.6	3.304
Surface area	Cluster: Lateral occipital, fusiform <sup>d</sup>	Right	4636.9	6,614	41.9	-69.8	5.6	4.483
	Cluster: Inferior parietal, lateral occipital <sup>d</sup>	Left	3861.5	6,219	-40.6	-71	32.6	4.059
MDS-UPDRS-III: Difference in correlation between groups								
Thickness	Cluster: Precentral, postcentral, paracentral, caudal middle frontal <sup>e</sup>	Left	4595.2	10,528	-31.3	-19.4	54.3	-4.049
	Cluster: Precentral <sup>e</sup>	Right	2429.5	5,638	11.1	-23.6	62.0	-3.454
Surface area	Cluster: Postcentral, precentral <sup>e</sup>	Left	2021.3	4,630	-47.0	-16.2	53.2	-5.280
	Cluster: Lateral occipital and fusiform <sup>e</sup>	Left	2116.1	2,832	-34.9	-86.3	-4.9	-2.984
	Cluster: Inferior parietal <sup>e</sup>	Left	1810.9	2,952	-36.3	-74.5	31.1	-2.862
	Cluster: Inferior temporal, fusiform, lingual <sup>e</sup>	Right	2367.9	4,074	40.8	-9.9	-24.8	-2.745
	Cluster: Lateral and medial orbitofrontal, superior frontal <sup>e</sup>	Right	2936.6	4,437	14.4	30.2	-17.4	-2.316
MoCA: Correlation analysis in iRBD								
Thickness	Cluster: Inferior, middle, superior temporal cortex, fusiform, lingual, entorhinal <sup>d</sup>	Right	7239.5	11,827	40.8	-41.8	-13.4	4.183
	Cluster: Insula, pars opercularis, rostral middle frontal, lateral orbitofrontal <sup>d</sup>	Left	5111.6	11,651	-41.0	-0.5	14.4	4.038
	Cluster: Fusiform and lingual <sup>d</sup>	Left	2277.5	3,100	-40.6	-61.8	-7.9	3.519
	Cluster: Insula, banks of STS, lateral orbitofrontal, pars opercularis <sup>d</sup>	Right	3774.7	9,208	43.1	-18.3	18.1	2.596

Results were corrected with Monte-Carlo simulation at  $p < 0.05$  with age, sex, and site entered as covariates, as well as total intracranial volume for surface area analysis. Clusters are listed by the strongest -log<sub>10</sub> p-value.

<sup>a</sup>iRBD < Controls.

<sup>b</sup>iRBD > Controls.

<sup>c</sup>Negative association.

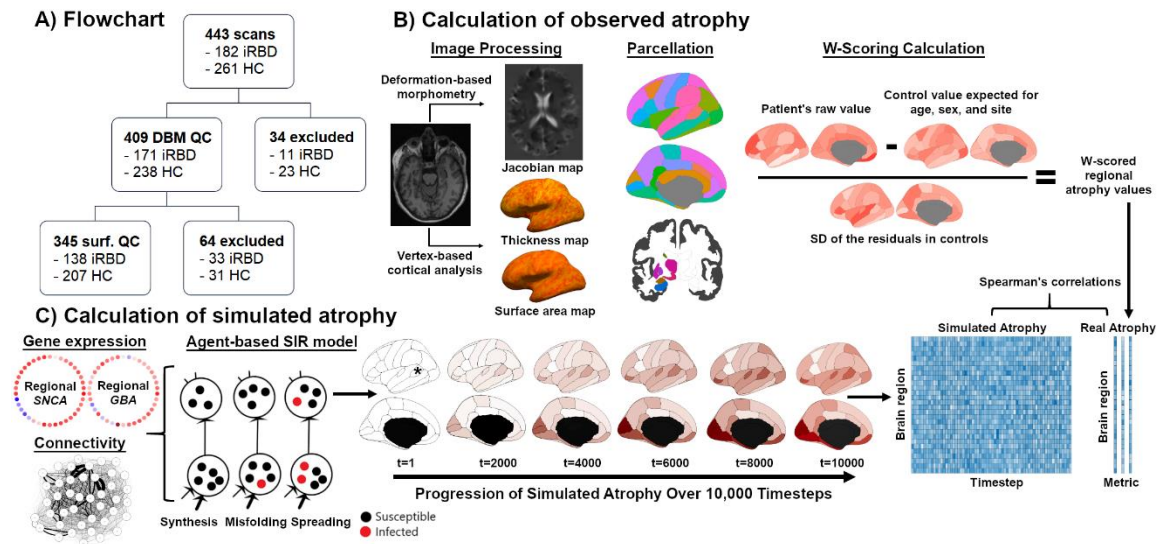
<sup>d</sup>Positive association.

<sup>e</sup>Stronger association in iRBD patients compared to controls.

iRBD = isolated REM sleep behaviour disorder; MDS = Movement Disorders Society; MoCA = Montreal Cognitive Assessment; STS = superior temporal sulcus; UPDRS-III = Unified Parkinson's Disease Rating Scale, motor examination.

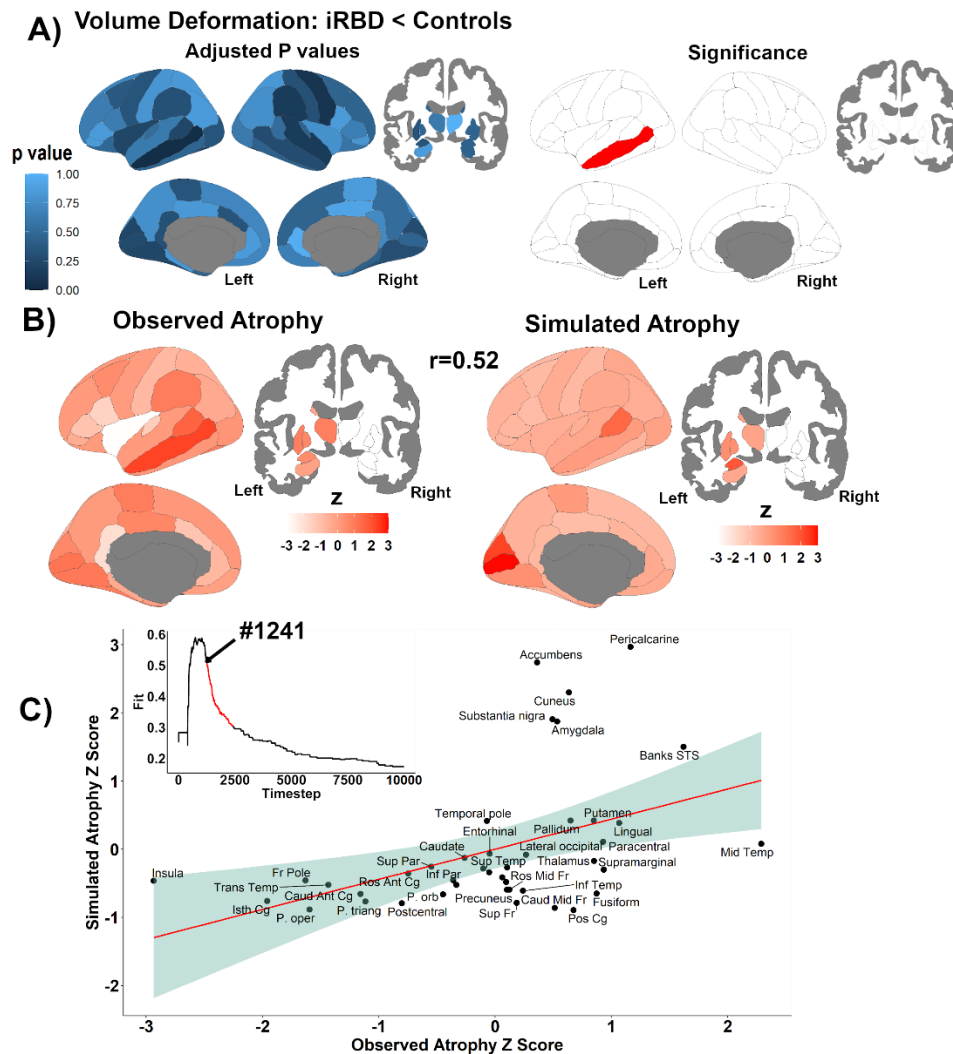
## Figure legends

**Figure 1 Demographics and clinical variables of iRBD and controls.**



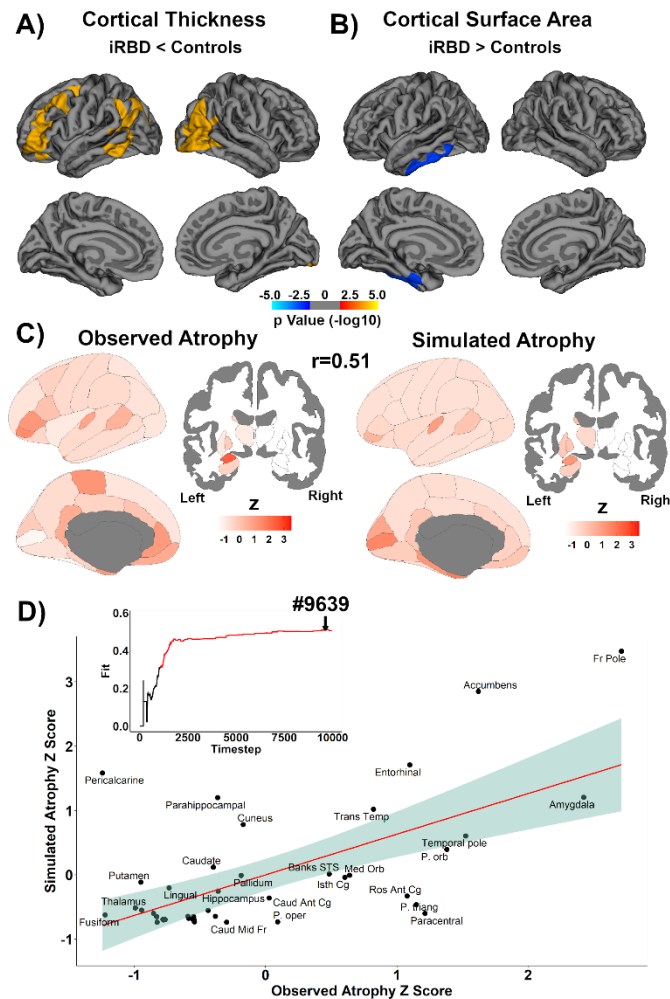
(A) A flowchart of the different cohorts included in this study. (B) Overview of the study protocol for quantifying brain atrophy in iRBD. Deformation-based morphometry and vertex-based cortical surface analysis were performed to generate Jacobian and cortical thickness and surface maps. These were parcellated and *W*-scored to correct for the effects of age, sex, and site seen in controls. These regional values were the atrophy patterns to recreate. (C) The spread of alpha-synuclein in the brain was simulated in silico using the agent-based SIR model based on structural connectomics and *SNCA* and *GBA* gene expression. The simulation was iterated 10,000 times, with brain atrophy being simulated at each timestep. These patterns were correlated with the observed atrophy patterns to assess if the model recreated atrophy. HC = healthy controls; iRBD = isolated REM sleep behaviour disorder; QC = quality control; SD = standard deviation; SIR = Susceptible-Infected-Removed.

**Figure 2 The model recreates the pattern of tissue deformation of iRBD.**



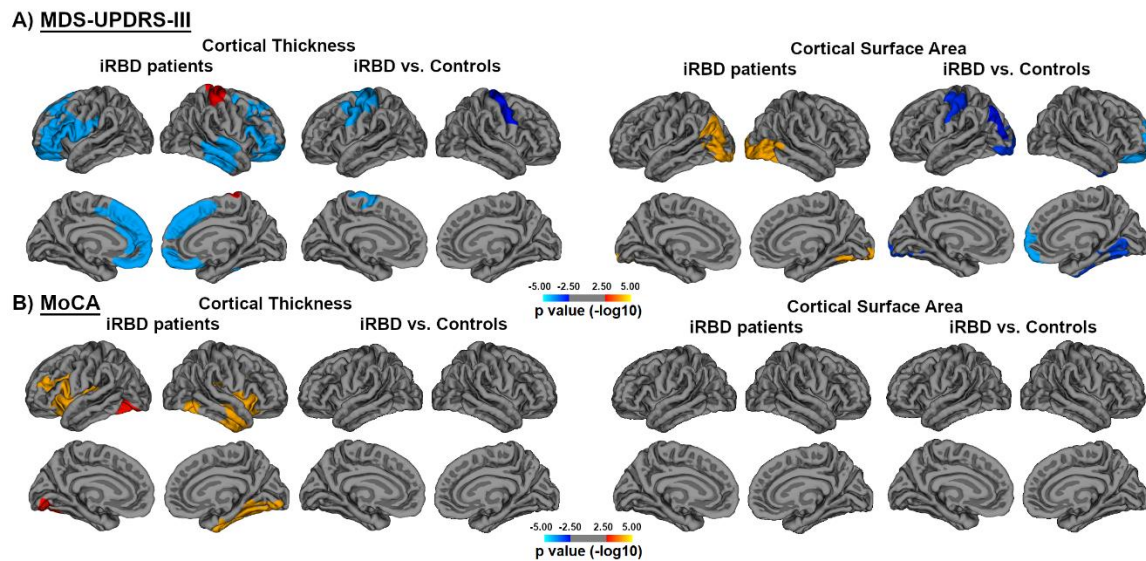
(A) Patients with iRBD showed significant volume decreases compared to controls (left: spatial distribution of FDR-adjusted  $p$ -values, right: significant differences after FDR-correction). (B) The pattern of volume loss in iRBD (left) was recreated by the model (right). For visualization purposes, atrophy  $W$ -scores were  $z$ -scored to ease comparability of scales; positive  $z$  scores represented greater atrophy. (C) The subplot shows the progression of the fit between atrophy patterns until the peak at timestep #1241 (arrow). The main scatterplot shows the  $z$ -scored values of observed and simulated atrophy at the peak fit for the 42 regions. Scales were adjusted such that higher scores represented greater atrophy. FDR = false discovery rate; iRBD = isolated REM sleep behaviour disorder.

**Figure 3 The model recreates the pattern of cortical thinning of iRBD.**



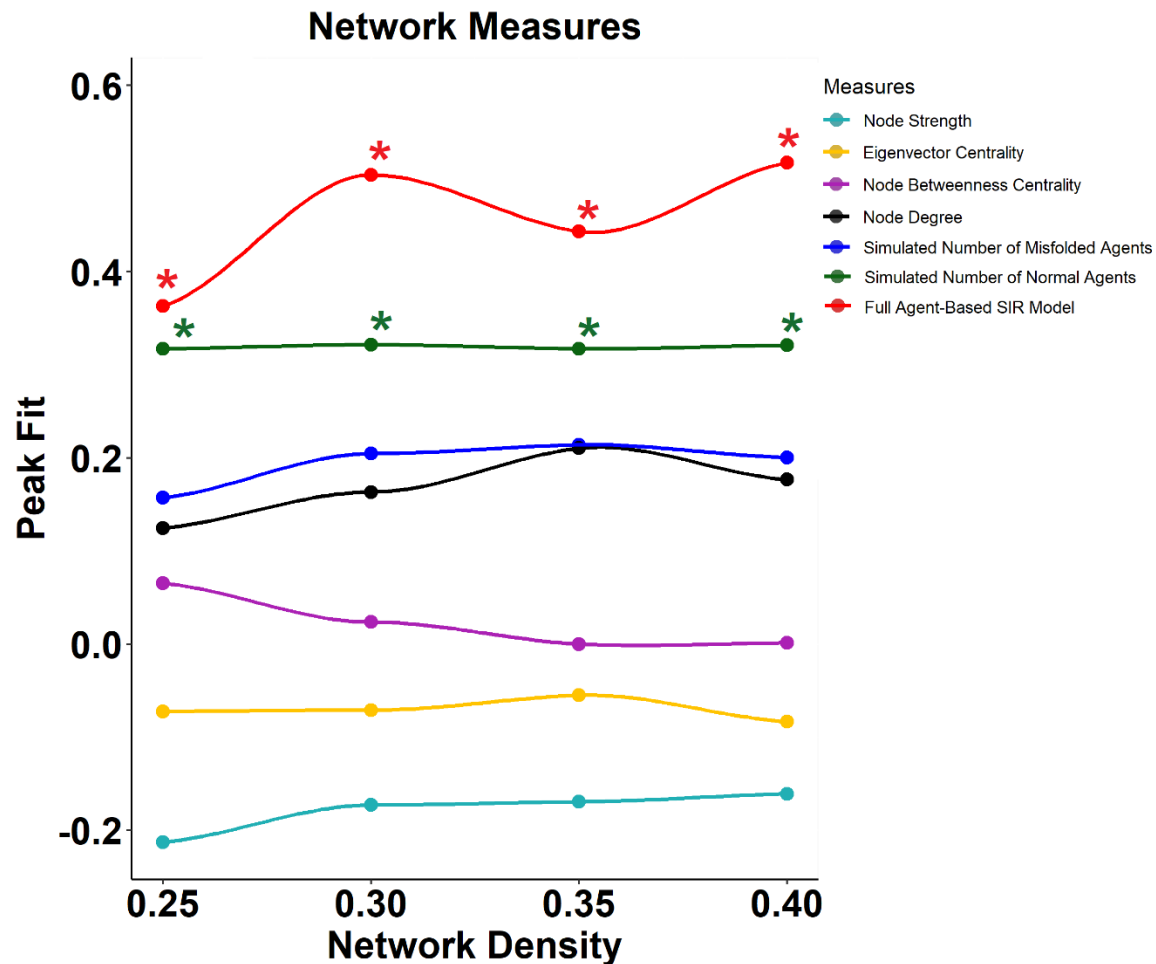
Patients with iRBD showed cortical thinning (A) and increased surface area (B) compared to controls. The colour bar indicates the statistical significance on a logarithmic scale of  $p$ -values ( $-\log_{10}$ ), with red-yellow areas showing significant decreases in iRBD and blue areas showing increases in iRBD. (C) The pattern of cortical thinning in iRBD (left) was recreated by the model (right). For visualization purposes, atrophy  $W$ -scores were  $z$ -scored to ease comparability of scales; positive  $z$  scores represented greater atrophy; positive  $z$  scores represent greater atrophy. (D) The subplot shows the progression of the fit between atrophy patterns until the peak at timestep 9,639 (arrow). The main scatterplot shows the  $z$ -scored values of observed and simulated atrophy at the peak fit for the 41 regions. Scales were adjusted such that higher scores represented greater atrophy. iRBD = isolated REM sleep behaviour disorder.

**Figure 4 Correlation analyses between cortical surface and motor and cognitive variables.**



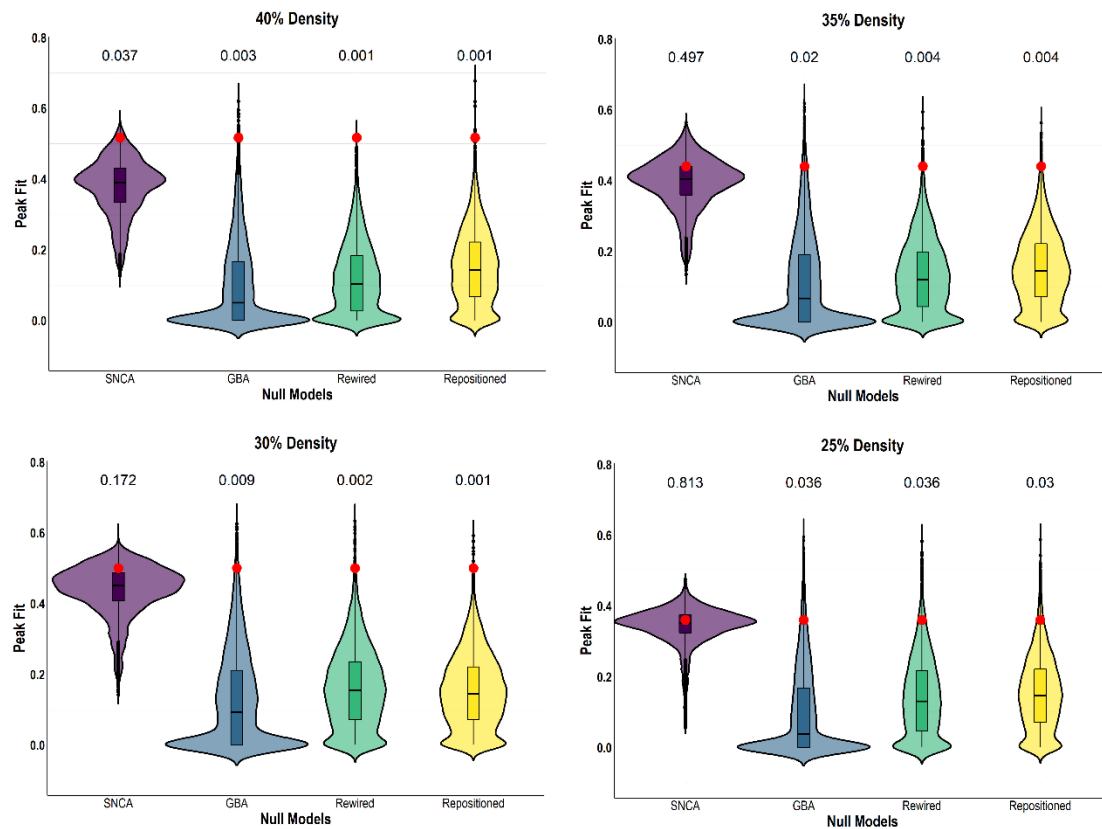
Results of the general linear models showing the vertices where a significant correlation was found with the MDS-UPDRS-III (**A**) and MoCA (**B**) in iRBD patients and the vertices where the slopes between the structural metric and these scores significantly differed between patients and controls. The colour bar indicates the statistical significance on a logarithmic scale of  $p$ -values ( $-\log_{10}$ ;  $\pm 1.3$  corresponding to  $p < 0.05$  corrected for multiple comparisons by Monte Carlo cluster-wise simulation), with red-yellow areas showing positive associations in iRBD and blue areas showing negative associations in iRBD. For comparisons of correlation, blue clusters represent stronger correlations in iRBD compared to controls. iRBD = isolated REM sleep behaviour disorder; MDS = Movement Disorders Society; MoCA = Montreal Cognitive Assessment; UPDRS-III = Unified Parkinson's Disease Rating Scale, part III.

**Figure 5 Simulated atrophy outperforms network and other model-derived measures.**



The highest peak fits found when recreating the deformation-based morphometry-derived tissue deformation pattern were found when using the simulated atrophy measure generated by the full agent-based SIR model. Asterisks represent the significant correlations between the observed pattern of atrophy and the different network and model-derived measures. SIR = Susceptible-Infected-Removed.

**Figure 6 Connectivity and gene expression shape the deformation-based morphometry-derived atrophy pattern.**



Violin plots comparing the original peak fits between atrophy patterns (red dots) to the average peak fits derived from null models in which network topology (“Rewired”), network geometry (“Repositioned”), *SNCA* expression (“SNCA”), and *GBA* expression (“GBA”) was randomly shuffled across regions. Unbiased Monte-Carlo estimates of the exact *p*-value were computed and reported above the plots. Comparisons with null models were performed for each connection density.

## Supplementary material

**Supplementary Table I Demographics of the different cohorts.**

Cohort	Group	Total number	Age (SD)	Sex, n (% men)	MDS-UPDRS-III	MoCA
Paris	iRBD	59	67.42 ± 6.16	52 (88)	8.47 ± 6.68	26.78 ± 2.79
Paris	Controls	57	65.94 ± 8.51	45 (79)	3.98 ± 4.77	27.51 ± 2.16
Montreal	iRBD	48	65.83 ± 6.43	37 (77)	4.31 ± 3.62 <sup>a</sup>	25.93 ± 2.72
Montreal	Controls	35	64.97 ± 7.13	21 (60)	-	28.17 ± 1.40
Sydney	iRBD	30	68.42 ± 7.24	27 (90)	11.58 ± 7.45	26.42 ± 3.34
Sydney	Controls	26	70.81 ± 6.22	17 (65)	-	-
Aarhus	iRBD	18	68.72 ± 8.22	15 (83)	1.11 ± 1.45	27.11 ± 1.97
Aarhus	Controls	20	67.90 ± 5.76	15 (75)	-	27.05 ± 2.12
PPMI cohort	iRBD	27	70.86 ± 5.32	21 (78)	5.11 ± 5.64	25.18 ± 4.51
PPMI cohort	Controls	123	66.07 ± 8.18	97 (79)	1.43 ± 2.46	28.15 ± 1.14

Data are presented as mean ± SD.

<sup>a</sup>Fahn & Elton UPDRS-III version.<sup>82</sup>

iRBD = isolated REM sleep behaviour disorder; MDS = Movement Disorders Society; MoCA = Montreal Cognitive Assessment; PPMI = Parkinson's Progression Markers Initiative; SD = standard deviation; UPDRS-III = Unified Parkinson's Disease Rating Scale, motor examination.

**Supplementary Table 2 Results of deformation-based morphometry between iRBD patients and controls.**

Region	iRBD (mean $\pm$ SD)	Controls (mean $\pm$ SD)	Beta coefficient	p-value	Adjusted p-value for FDR
<b>Left hemisphere</b>					
Middle temporal cortex <sup>a</sup>	1.008 (0.053)	1.019 (0.050)	-0.016	0.001	0.045
Cuneus <sup>b</sup>	1.007 (0.079)	1.014 (0.082)	-0.018	0.030	0.274
Lingual gyrus <sup>b</sup>	1.015 (0.063)	1.022 (0.066)	-0.014	0.033	0.274
Fusiform gyrus <sup>b</sup>	1.024 (0.085)	1.028 (0.079)	-0.014	0.032	0.274
Banks STS <sup>b</sup>	0.976 (0.081)	0.988 (0.073)	-0.017	0.026	0.274
Insula <sup>b</sup>	1.013 (0.053)	0.999 (0.044)	0.011	0.030	0.274
Pericalcarine <sup>b</sup>	0.960 (0.082)	0.973 (0.090)	-0.018	0.043	0.286
Supramarginal	1.004 (0.052)	1.010 (0.050)	-0.010	0.062	0.325
Isthmus cingulate	0.991 (0.055)	0.979 (0.057)	0.011	0.066	0.326
Frontal pole	1.046 (0.052)	1.033 (0.056)	0.009	0.112	0.428
Precentral	1.029 (0.046)	1.031 (0.044)	-0.007	0.110	0.428
Paracentral	1.008 (0.081)	1.017 (0.079)	-0.013	0.119	0.428
Caudal anterior cingulate	0.979 (0.063)	0.970 (0.060)	0.010	0.127	0.428
Lateral occipital	1.029 (0.039)	1.032 (0.047)	-0.007	0.124	0.428
Putamen	0.916 (0.062)	0.925 (0.058)	-0.009	0.099	0.428
Amygdala	0.993 (0.082)	0.996 (0.071)	-0.011	0.106	0.428
Caudal middle frontal	1.019 (0.058)	1.025 (0.064)	-0.009	0.148	0.435
Entorhinal	1.047 (0.121)	1.044 (0.106)	-0.012	0.208	0.452
Caudate	1.027 (0.120)	1.013 (0.109)	0.015	0.204	0.452
Pallidum	0.913 (0.064)	0.923 (0.061)	-0.007	0.221	0.453
Inferior temporal	1.047 (0.090)	1.043 (0.078)	-0.007	0.230	0.454
Lateral orbitofrontal	1.001 (0.072)	0.999 (0.071)	-0.006	0.252	0.480
Temporal pole	1.015 (0.089)	1.014 (0.077)	-0.008	0.262	0.488
Transverse temporal	1.004 (0.083)	0.990 (0.081)	0.009	0.292	0.515
Thalamus	0.959 (0.059)	0.960 (0.055)	-0.005	0.384	0.614
Accumbens area	1.012 (0.070)	1.008 (0.064)	-0.005	0.387	0.614
Superior temporal	1.005 (0.041)	1.005 (0.045)	-0.004	0.399	0.621
Pars opercularis	1.024 (0.062)	1.016 (0.060)	0.005	0.429	0.652
Rostral middle frontal	1.024 (0.038)	1.026 (0.044)	-0.003	0.436	0.652
Superior frontal	1.014 (0.043)	1.017 (0.048)	-0.003	0.511	0.715
Medial orbitofrontal	1.012 (0.095)	1.005 (0.085)	-0.004	0.520	0.717
Precuneus	1.009 (0.060)	1.009 (0.056)	-0.003	0.587	0.771
Postcentral	1.025 (0.042)	1.023 (0.044)	-0.002	0.636	0.808
Parahippocampal	0.997 (0.067)	0.994 (0.068)	-0.003	0.659	0.814
Posterior cingulate	0.981 (0.050)	0.981 (0.048)	-0.002	0.690	0.828
Superior parietal	1.051 (0.057)	1.049 (0.051)	-0.002	0.713	0.843
Pars triangularis	1.024 (0.057)	1.017 (0.062)	0.002	0.749	0.850
Pars orbitalis	1.016 (0.048)	1.012 (0.052)	-0.001	0.766	0.858
Rostral anterior cingulate	0.945 (0.056)	0.943 (0.066)	0.001	0.812	0.870
Hippocampus	0.964 (0.050)	0.964 (0.051)	-0.001	0.818	0.870
Inferior parietal	1.032 (0.054)	1.032 (0.052)	-0.001	0.832	0.873
Substantia nigra	0.920 (0.056)	0.927 (0.054)	-0.001	0.889	0.911
<b>Right hemisphere</b>					
Precentral <sup>b</sup>	1.016 (0.045)	1.025 (0.048)	-0.015	0.002	0.090
Supramarginal <sup>b</sup>	1.000 (0.053)	1.009 (0.050)	-0.014	0.007	0.146
Superior temporal <sup>b</sup>	0.994 (0.051)	1.003 (0.047)	-0.014	0.007	0.146

Cuneus <sup>b</sup>	1.028 (0.080)	1.032 (0.081)	-0.017	0.036	0.274
Middle temporal <sup>b</sup>	1.010 (0.062)	1.017 (0.060)	-0.012	0.017	0.274
Lingual <sup>b</sup>	1.036 (0.064)	1.039 (0.067)	-0.013	0.044	0.286
Postcentral	1.022 (0.051)	1.029 (0.051)	-0.010	0.055	0.310
Fusiform	1.029 (0.088)	1.030 (0.083)	-0.012	0.055	0.310
Caudate	1.083 (0.164)	1.053 (0.144)	0.025	0.107	0.428
Parahippocampal	1.003 (0.063)	1.006 (0.057)	-0.008	0.133	0.429
Inferior temporal	1.056 (0.097)	1.052 (0.090)	-0.009	0.150	0.435
Amygdala	1.002 (0.074)	1.003 (0.068)	-0.009	0.147	0.435
Rostral middle frontal	1.015 (0.042)	1.019 (0.049)	-0.006	0.211	0.452
Superior frontal	1.024 (0.048)	1.028 (0.051)	-0.007	0.202	0.452
Caudal middle frontal	1.013 (0.066)	1.022 (0.071)	-0.010	0.169	0.452
Caudal anterior cingulate	0.990 (0.079)	0.978 (0.067)	0.010	0.215	0.452
Transverse temporal	0.977 (0.069)	0.981 (0.065)	-0.009	0.209	0.452
Putamen	0.920 (0.064)	0.928 (0.059)	-0.008	0.164	0.452
Pallidum	0.914 (0.060)	0.924 (0.057)	-0.007	0.204	0.452
Hippocampus	0.972 (0.051)	0.976 (0.048)	-0.007	0.174	0.452
Substantia nigra	0.921 (0.055)	0.931 (0.052)	-0.007	0.188	0.452
Pericalcarine	1.023 (0.091)	1.024 (0.095)	-0.011	0.232	0.454
Precuneus	1.026 (0.064)	1.027 (0.064)	-0.007	0.300	0.515
Temporal pole	1.022 (0.086)	1.020 (0.077)	-0.008	0.283	0.515
Banks STS	0.989 (0.083)	0.998 (0.072)	-0.008	0.297	0.515
Lateral orbitofrontal	1.002 (0.079)	0.996 (0.075)	-0.006	0.337	0.566
Lateral occipital	1.035 (0.046)	1.032 (0.051)	-0.004	0.385	0.614
Medial orbitofrontal	1.004 (0.087)	0.999 (0.078)	-0.005	0.458	0.652
Pars triangularis	1.000 (0.066)	1.003 (0.068)	-0.005	0.449	0.652
Entorhinal	1.068 (0.107)	1.061 (0.100)	-0.006	0.456	0.652
Isthmus cingulate	0.989 (0.059)	0.984 (0.060)	0.004	0.542	0.734
Inferior parietal	1.033 (0.049)	1.032 (0.049)	-0.003	0.580	0.771
Insula	0.973 (0.047)	0.974 (0.042)	-0.002	0.602	0.778
Pars orbitalis	1.006 (0.054)	1.001 (0.058)	-0.002	0.645	0.808
Superior parietal	1.049 (0.056)	1.049 (0.050)	-0.002	0.674	0.821
Pars opercularis	1.008 (0.073)	1.004 (0.066)	0.003	0.725	0.846
Frontal pole	1.048 (0.056)	1.041 (0.055)	0.002	0.745	0.850
Paracentral	1.045 (0.087)	1.040 (0.080)	-0.002	0.785	0.859
Accumbens area	1.008 (0.066)	1.001 (0.060)	-0.001	0.787	0.859
Posterior cingulate	0.986 (0.052)	0.981 (0.049)	0.001	0.888	0.911
Rostral anterior cingulate	0.965 (0.080)	0.962 (0.072)	0.0004	0.957	0.969
Thalamus	0.992 (0.065)	0.986 (0.062)	0.00005	0.993	0.993

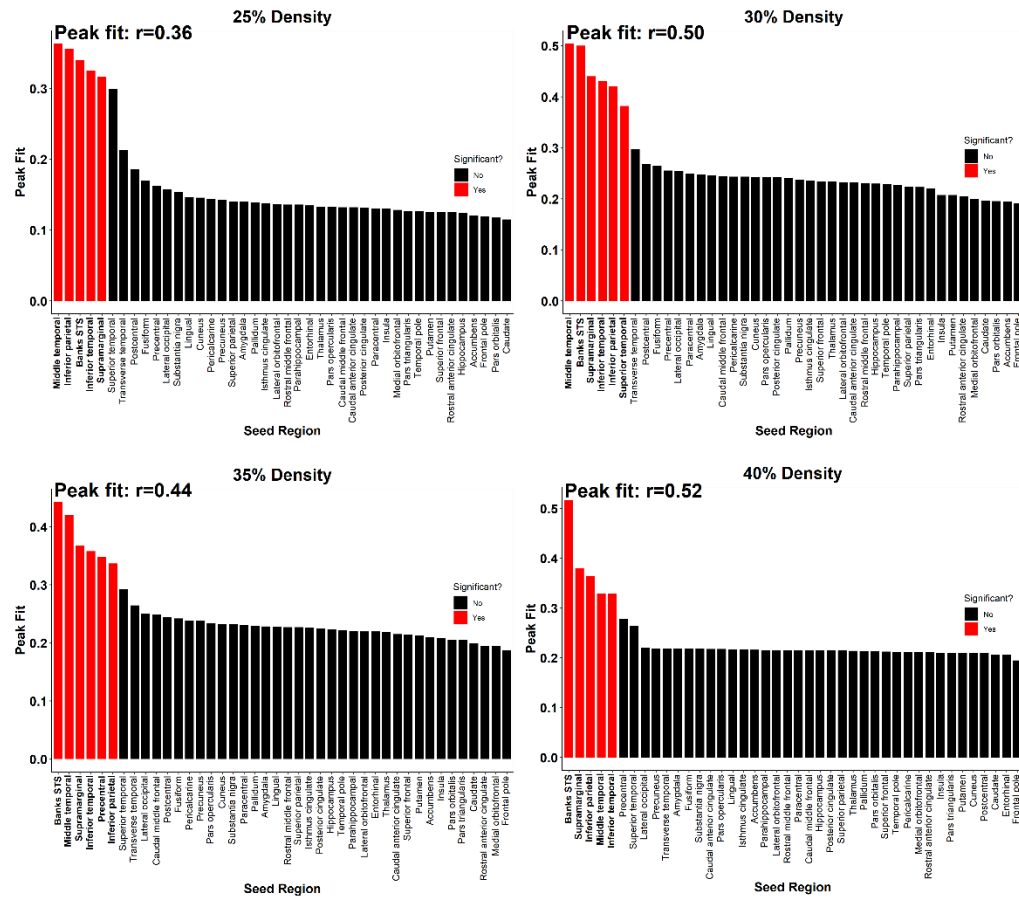
Regions are ordered separately for each hemisphere from the lowest FDR-adjusted *p*-values to the highest.

<sup>a</sup>Significant when using the FDR-adjusted *p*-values.

<sup>b</sup>Significant when using an uncorrected *p*-value of <0.05.

FDR = false discovery rate; iRBD = isolated REM sleep behaviour disorder; SD = standard deviation; STS = superior temporal sulcus.

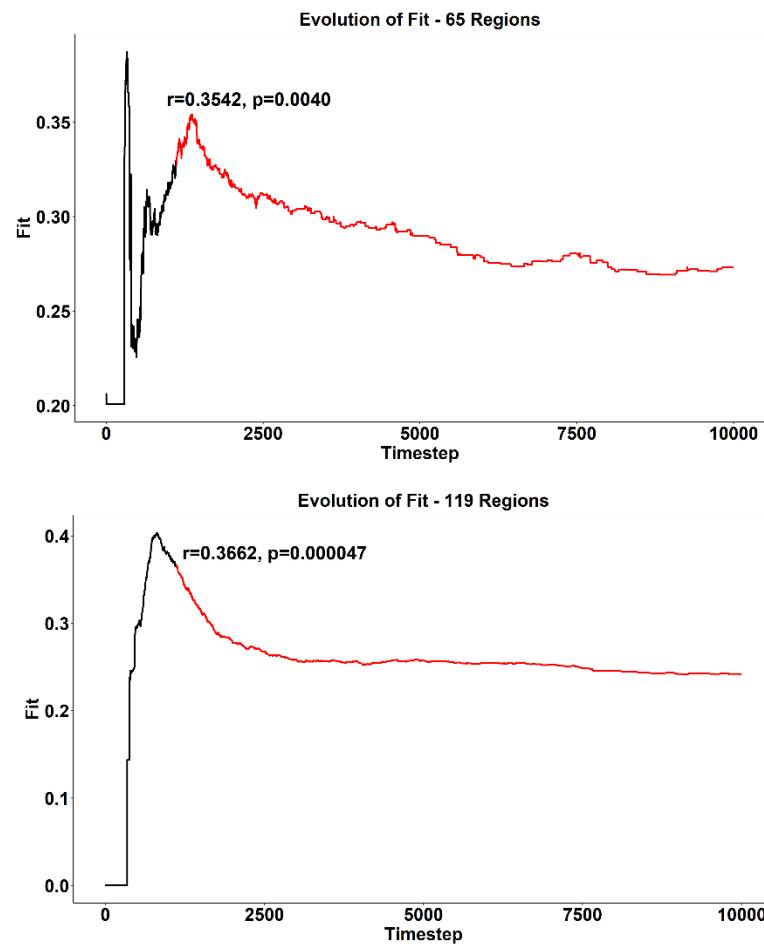
**Supplementary Figure 1.** The model recreated deformation-based morphometry-derived tissue deformation of iRBD at different network densities.



The atrophy simulated by the model using connection densities varying from 25% to 40% always recreated the pattern of tissue deformation observed in iRBD. Red columns represent the seed regions that led to a significant recreation of tissue deformation.

iRBD = isolated REM sleep behaviour disorder; STS = superior temporal sulcus.

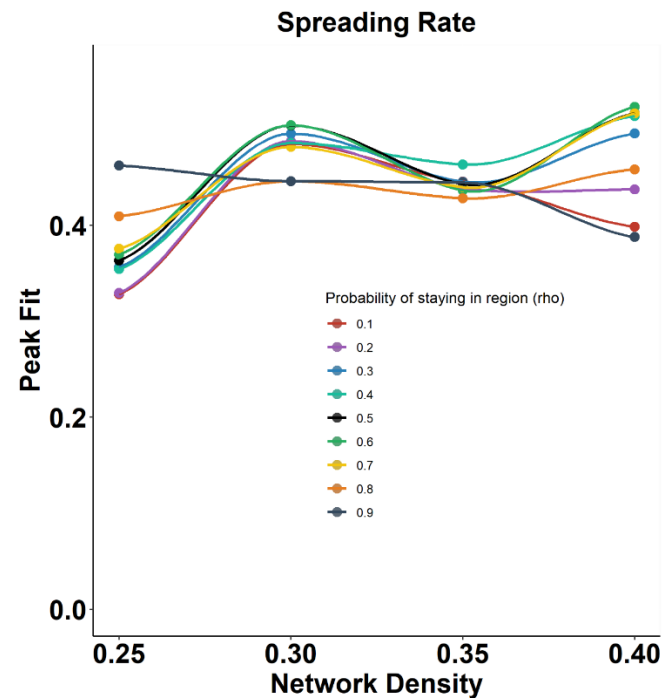
**Supplementary Figure 2.** The model recreated the deformation-based morphometry-derived tissue deformation pattern using finer brain parcellations.



The model also recreated the deformation-based morphometry-derived tissue deformation pattern of iRBD when simulating the spread of agents using brain parcellations of 65 and 119 regions.

iRBD = isolated REM sleep behaviour disorder.

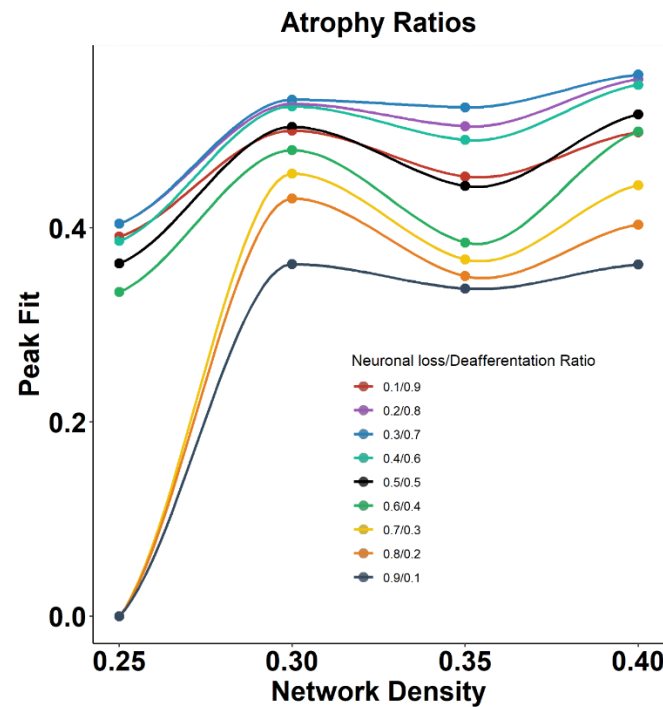
**Supplementary Figure 3.** The model recreated the deformation-based morphometry-derived tissue deformation pattern at various spreading rates.



The model recreated the deformation-based morphometry-derived tissue deformation pattern of iRBD when using different  $\rho$  values (i.e., the probability that an agent remained in a region instead of leaving the region) from 0.1 to 0.9. The main analyses performed in the article used  $\rho=0.5$ .

iRBD = isolated REM sleep behaviour disorder.

**Supplementary Figure 4.** The model recreated the deformation-based morphometry-derived tissue deformation pattern at various atrophy ratios.



The model recreated the deformation-based morphometry-derived tissue deformation pattern of iRBD when using different weights for neuronal loss and deafferentation in the quantification of the model's simulated atrophy measure. The main analyses performed in the paper used equal weights for neuronal loss and deafferentation ( $k=0.5$ ).

iRBD = isolated REM sleep behaviour disorder.